The organization of intracortical connections by layer and cell class in the mouse brain

Julie A. Harris*[1], Stefan Mihalas[1], Karla E. Hirokawa[1], Jennifer D. Whitesell[1], Joseph E. Knox[1], Amy Bernard[1], Phillip Bohn[1], Shiella Caldejon[1], Linzy Casal[1], Andrew Cho[1], David Feng[1], Nathalie Gaudreault[1], Charles R. Gerfen[2], Nile Graddis[1], Peter A. Groblewski[1], Alex Henry[1], Anh Ho[1], Robert Howard[1], Leonard Kuan[1], Jerome Lecoq[1], Jennifer Luviano[1], Stephen McConoghy[1], Marty T. Mortrud[1], Maitham Naeemi[1], Lydia Ng[1], Seung W. Oh[1], Benjamin Ouellette[1], Staci A. Sorensen[1], Wayne Wakeman[1], Quanxin Wang[1], Ali Williford[1], John W. Phillips[1], Allan Jones[1], Christof Koch[1], and Hongkui Zeng[1]

[1]Allen Institute for Brain Science
[2]Laboratory of Systems Neuroscience, National Institute of Mental Health
*Correspondence should be addressed to J.A.H. (julieha@alleninstitute.org)

Abstract

The mammalian cortex is a laminar structure composed of many cell types densely interconnected in complex ways. Recent systematic efforts to map the mouse mesoscale connectome provide comprehensive projection data on interareal connections, but not at the level of specific cell classes or layers within cortical areas. We present here a significant expansion of the Allen Mouse Brain Connectivity Atlas, with ~1,000 new axonal projection mapping experiments across nearly all isocortical areas in 49 Cre driver lines. Using 13 lines selective for cortical layer-specific projection neuron classes, we identify the differential contribution of each layer/class to the overall intracortical connectivity patterns. We find layer 5 (L5) projection neurons account for essentially all intracortical outputs. L2/3, L4, and L6 neurons contact a subset of the L5 cortical targets. We also describe the most common axon lamination patterns in cortical targets. Most patterns are consistent with previous anatomical rules used to determine hierarchical position between cortical areas (feedforward, feedback), with notable exceptions. While diverse target lamination patterns arise from every source layer/class, L2/3 and L4 neurons are primarily associated with feedforward type projection patterns and L6 with feedback. L5 has both feedforward and feedback projection patterns. Finally, network analyses revealed a modular organization of the intracortical connectome. By labeling interareal and intermodule connections as feedforward or feedback, we present an integrated view of the intracortical connectome as a hierarchical network.

31 Cognitive processes and voluntary control of behavior originates in the isocortex. Understanding how
32 incoming sensory information is processed, integrated with past experiences and current states to
33 generate memories, percepts, and motor outputs requires knowledge of the anatomical patterns and rules
34 of connectivity between cortical areas. Connectomes, complete descriptions of the wiring in a brain[1], exist
35 at different levels of spatial granularity (micro-, meso-, and macro-scale), each revealing different
36 principles of brain organization. At the mesoscale[2], connectivity is described at the level of cell
37 populations, classes, or types. Recently, several mesoscale cortical connectomes have been produced,
38 either through new systematic data generation[3–5], or via expert collation of historical tract tracing
39 literature[6–8]. Common organizational features of cortical connectivity in both rodent and macaque have
40 been distilled from these datasets, often using graph theoretical approaches to describe network
41 architecture[9,10]. For example, areas have unique patterns of connections (*i.e.,* a "fingerprint"), connection
42 strengths follow a log-normal distribution spanning > 4 orders of magnitude[4,5], and networks display high
43 clustering coefficients, with some highly connected nodes ("hubs")[4]. Finally, the organization of cortical
44 areas is modular, with distinct modules corresponding to specific functions[3,11].

45 Organizational schemes other than modular networks have previously been applied to cortical
46 connections to explain information flow and processing. Specifically, the concept of a cortical
47 hierarchy[12,13] has been useful for understanding computational and architectural properties of the cortex
48 and has inspired the development of neuronal network methods in machine vision[14]. These schemes
49 (modular and hierarchical) are not mutually exclusive, and the actual organization of the cortex involves
50 both types.

51 So far, the available mesoscale datasets are not clearly differentiated from macroscale connectivity in that
52 the experiments and analyses focus on connections between areas, treating them as more or less
53 homogenous regions. Data are often generated using tracers that cover entire cortical columns. In the
54 first phase of the Allen Mouse Brain Connectivity Atlas, injections were intentionally placed at multiple
55 depths within a cortical area in one experiment to infect all neurons across the cortical layers[4]. However,
56 each cortical region is composed of a heterogeneous mix of distinct cell types. Perhaps the most
57 characteristic feature of the isocortex is its organization into six layers. Within these layers, distinct cell
58 types exist that can be further differentiated based on morphological, electrophysiological, and
59 transcriptional properties[15–17]. Specific long-distance connectivity patterns are associated with excitatory
60 cell populations or genetically-identified types in each layer[16,18]. Long-distance axon projections are
61 commonly used to classify excitatory neurons into three main classes; intratelencephalic (IT), pyramidal
62 tract (PT), and corticothalamic (CT). Axons from IT neurons project to both ipsilateral and contralateral
63 cortex and striatum. PT neurons target subcortical structures, including those in the spinal cord, medulla,
64 pons, and midbrain, and can send branches to ipsilateral cortex, striatum, and thalamus. CT neurons
65 project to ipsilateral thalamus. IT neurons are found across all layers containing excitatory cells (L2/3, L4,
66 L5, L6), while PT neurons locate to L5 and CT neurons to L6[19,20]. Projections from these major classes to
67 different target regions suggests that they play distinct roles in information processing.

68 Experimental access to cortical cells in different layers and classes is feasible due to the generation of
69 diverse Cre driver transgenic mouse lines[21–24]. By taking advantage of them, we significantly expanded
70 upon our previously published Allen Mouse Brain Connectivity Atlas (http://connectivity.brain-map.org[4,25])
71 adding ~ 1,000 new experiments in the cortex. Here we present this enhanced online resource of
72 projection data from cortical cell classes defined by laminar position and brain-wide projection patterns.
73 We first describe the macroscale organization of cortical connectivity into six network modules and the
74 unique patterns of intracortical connectivity from each source. Then, we show the contribution of each
75 layer-specific projection neuron class to the complete intracortical projection pattern for a given region.
76 We observe diverse axon lamination patterns in cortical targets related to the layer of origin and
77 projection neuron class labeled by each Cre line. These patterns are both similar to and different from
78 previous anatomical patterns derived from anterograde tracing to define hierarchical position (feedforward
79 and feedback) in the visual cortex of primates[12] and rodents[26]. Using the cell layer/class-based projection
80 patterns, we ordered 37 of 43 isocortical areas into hierarchical positions. We also ordered the network

81 modules identified here; from bottom to top: somatomotor, temporal, visual, medial, anterolateral, and
82 prefrontal cortex.

83 ## Results

84 *Data generation and characterization of Cre driver lines for layer- and cell class-selective mapping*
85 Our pre-existing pipeline for generation and quantification of projection mapping data across the entire
86 brain[4] was used in this study, with some modifications. In brief, in Oh et al., 2014 we used only wild-type
87 C57BL/6J mice injected with a Cre-independent tracer, rAAV2/1.hSyn.EGFP.WPRE. Here, we used
88 transgenic Cre driver mice. Most Cre mice were injected with a Cre-dependent rAAV tracer,
89 rAAV2/1.pCAG.FLEX.EGFP.WPRE. A subset had a duplicate injection of an rAAV with a synaptophysin-
90 EGFP fusion transgene in place of the cytoplasmic EGFP, rAAV2/1.pCAG.FLEX.SypEGFP.WPRE.
91 Results from these two tracers were highly and significantly correlated for injections in close spatial
92 proximity (**Supplemental Figure 1**). Thus, we included the SypEGFP datasets when indicated for
93 analyses of connectivity patterns from given source areas. Following tracer injections, brains were imaged
94 using serial 2-photon tomography[27] (STP) at high x-y resolution (0.35 μm x 0.35 μm) every 100 μm, after
95 which the images underwent QC and manual annotation of injection sites, followed by signal detection
96 and registration to the Allen Mouse Brain Common Coordinate Framework (CCF), our fully annotated 3D
97 volumetric reference atlas, for subsequent data analyses, data visualization, and public release to our
98 web portal[28].

99 Our goal for expanding on the Allen Mouse Brain Connectivity Atlas (http://connectivity.brain-map.org)
100 was to create a comprehensive map of all inter-areal projections originating from neurons of different cell
101 classes within a given source. Forty-nine Cre driver lines (**Supplemental Table 1**) entered the pipeline for
102 cortical projection mapping after initial anatomical characterization of transgene expression across the
103 brain using *in situ* hybridization[23] (http://connectivity.brain-map.org/transgenic). These driver lines have
104 either pan-layer Cre expression (e.g. Emx1-IRES-Cre), layer-selective Cre expression, or Cre expression
105 driven by inhibitory neuron-specific promotors. Layer-selectivity data for 15 lines are summarized in the
106 second row ("Layer") of **Figure 1a**. Data used to determine layer-selectivity can be found in
107 **Supplemental Figure 2**. Many Cre lines showed relatively even distribution of expression across the
108 entire isocortex, but we also saw gradients and area-restricted expression patterns which were used to
109 choose appropriate locations for tracer injections.

110 Across the 50 mouse lines (49 Cre and wild type), we generated a total of 1,082 experiments
111 (**Supplemental Tables 1 and 2**). Most of these experiments (n=850) used 15 out of 50 lines (14 Cre and
112 wild type). **Figure 1a** shows the 850 tracer experiments by line and cortical area. Mouse isocortex is
113 parcellated into 43 areas in the Allen CCF, visualized here in two ways. A top-down view (**Figure 1b**), and
114 a flattened view of the entire right hemisphere of cortex, to show all cortical areas in one 2D image
115 (**Figure 1c**). Locations of the injections' centroids (x,y,z voxel coordinate after registration to the Allen
116 CCF) for all 1,082 experiments are plotted onto the cortical surface flat map in **Figure 1d**. Left side
117 injections were plotted here on the right hemisphere to visualize completeness of areal coverage. All
118 subsequent analyses refer to "ipsilateral" and "contralateral" relative to the side of injection. Of the 43
119 cortical areas, only 10 had 5 or fewer experiments. These areas (FRP, AIv, SSp-un, AIp, GU, VISC,
120 AUDv, TEa, PERI, and ECT) were generally harder to target due to their size (SSp-un) or their location in
121 very ventral or lateral regions (see **Figure 1c**). Abbreviations for isocortex regions are included in
122 **Supplemental information**.

123 Data from all 1,000+ experiments in the isocortex are publicly available at the Allen Mouse Brain
124 Connectivity Atlas data portal (http://connectivity.brain-map.org/). Individual experimental IDs and
125 associated metadata are listed in **Supplemental Table 2.**

126 We visually inspected the brain-wide axonal projection patterns and classified all 1000+ experiments
127 based on the principles described above for defining IT, PT, and CT neuron classes. Each experiment
128 was manually assigned to one of five groups (**Supplemental Figure 3a-e**); (a) IT PT CT, when labeled

3

129 axons were observed in all regions of interest (ipsilateral and contralateral cortex and striatum, and
130 subcortical and thalamic projections), (b) IT, when labeled axons were restricted to ipsilateral and
131 contralateral cortex and striatum, (c) PT, when labeled axons were ipsilateral and subcortically-projecting,
132 (d) CT, when labeled axons projected almost exclusively to thalamus, and (e) local, when no (or few)
133 long-distance (*i.e.,* outside of the source area) axons were seen. The consensus of results across all
134 sources for each mouse line is shown in the "projection class row" of **Figure 1a.** More details can be
135 found in **Supplemental Figure 3f**, which shows both the consensus projection neuron class for each Cre
136 line and the class per source mapped within a Cre line. A subset of Cre lines are highly selective for IT,
137 PT, or CT neurons, consistent with previous characterizations[22,29,30]. Most lines label neurons of the same
138 projection class independent of the source area, but there are interesting exceptions. For example, L5
139 cells expressing Cre in the Chrna2-Cre_OE25 line are of the PT class in 14 of the 19 sources tested, but
140 only locally projecting neurons are labeled in other sources (e.g. VISp) in this line. The manual
141 assignment of experiments and Cre lines to projection neuron classes was also validated through
142 unsupervised hierarchical clustering analysis of informatically-derived whole brain projection volumes in
143 relevant major brain divisions (**Supplemental Figure 4**).

144 Together, the characterization of layer- and projection neuron class-selectivity for each Cre line enabled
145 us to choose a core set of the best lines for comprehensively mapping connectivity from known classes of
146 projection neurons in each cortical layer. These 13 lines, together with experiments in wild type mice
147 (C57BL/6J) and the pan-layer Emx1-IRES-Cre line were used to identify all intracortical projections.
148 These lines include L2/3 IT (Cux2-IRES-Cre and Sepw1-Cre_NP39), L4 IT (Nr5a1-Cre, Scnn1a-Tg3-Cre,
149 and Rorb-IRES-Cre), L5 IT (Tlx3-Cre_PL56), L5 PT (A93-Tg1-Cre, Chrna2-Cre_OE25, Efr3a-
150 Cre_NO108, Sim1-Cre_KJ18), L5-all classes (Rbp4-Cre_KL100), and L6 CT (Ntsr1-Cre_GN220, Syt6-
151 Cre_KI148). One class for which we did not identify a suitable Cre line is L6 IT[16].

152 *Intracortical connections are organized into modules*
153 Cortical areas have distinct patterns (targets and weights) of corticocortical projections revealed through
154 anterograde tracing in wild type mice[3,4] (**Figure 2**). However, similarities between output patterns of some
155 areas are also obvious when viewing the anatomical data spatially (**Figure 2a**) or the connection
156 strengths in matrix form (**Figure 2b**). The matrix shows the output of a new data-driven model, which, for
157 the isocortex, was based on 122 injections in wild type mice[31]. This model differs from our previously
158 published model[4] in that it is built through spatial interpolation at the voxel level (100 μm), rather than for
159 each brain region, enabling the recovery of high spatial resolution for connectivity strengths between
160 voxels. The voxel-based connection strengths were then unionized for every isocortical region annotated
161 in the Allen CCF (n=43, **Figure 1**). **Figure 2b** shows the ipsilateral intracortical connectivity matrix.

162 We analyzed the network structure of this ipsilateral matrix using the Louvain algorithm from the Brain
163 Connectivity Toolbox[32]. This algorithm maximizes a modularity metric (Q) to identify groups of nodes
164 (cortical areas) most densely connected to each other compared to a randomized network. Q quantifies
165 the fraction of connections inside modules minus the fraction of connections expected inside the same
166 modules if the network were connected randomly, *i.e.,* Q=0 has no more intramodule connections than
167 expected by chance, while Q>0 indicates a network with some community structure.

168 To identify stable modules, we systematically varied the spatial resolution parameter, γ, from 0 to 2.5, and
169 measured Q at each value of γ, compared to Q for a shuffled network. Increasing γ enables the detection
170 of more modules, each containing fewer nodes[8,33]. The mouse cortex showed significant modularity (Q>Q
171 for the shuffled network) for every value of γ above 0.3. Between 1 and 14 modules were identified across
172 this range (**Figure 2b**, colors on left axis). For subsequent analyses, we chose to focus on the modules
173 identified at γ=1.3 (Q=0.37). This value of γ corresponds to the midpoint between no modules at all, and
174 the γ value of 2.5 where modules contain single regions. It is also the γ level where the difference
175 between Q and $Q_{shuffled}$ was at its peak (0.2224±0.0021), although this difference was relatively stable

176   between γ=1 and γ=1.8 (0.2187±0.0048 at γ=1, 0.2020±0.0009 at γ=1.8). The network is divided into six
177   modules at this point, containing 5-8 regions each.

178   We named the six modules based on the cortical areas assigned to each; (1) **Prefrontal**: FRP, MOs,
179   ACAd, ACAv, PL, ILA, ORBl, ORBm, ORBvl (2), **Anterolateral**: AId, AIv, AIp, GU, VISC, (3)
180   **Somatomotor:** SSs, SSp-bfd, SSp-tr, SSp-ll, SSp-ul, SSp-un, SSp-n, SSp-m, MOp, (4) **Visual**: VISal,
181   VISrl, VISl, VISp, VISpl, VISli, VISpor, (5) **Medial**: RSPagl, RSPd, RSPv, VISa, VISam, VISpm, and (6)
182   **Temporal**: AUDd, AUDp, AUDpo, AUDv, TEa, PERI, and ECT. Although we use these six modules for
183   subsequent analyses, and to describe the organization of cortical areas based on connections, it should
184   be emphasized that there are other, equally valid, levels of organization that could be chosen. For
185   example, there is a four-module solution at γ=1.0 that results in prefrontal, somatomotor, visual, and
186   temporal modules, in which the anterolateral areas are not split from somatomotor areas, and medial
187   regions are still grouped with the visual areas. The spatial relationships between areas in these six
188   modules are shown in the 3D renderings of brain areas in the Allen CCF in **Figure 2c**. There is a clear
189   spatial component to the module assignment, in that nearby areas often belong to the same module. This
190   is perhaps not surprising given that connectivity strengths drop as a function of distance[4,34], but does not
191   negate the likely importance of long-distance intermodule connections for integration and information
192   flow. The network of connections within and between all modules and nodes was also visualized using a
193   force-directed layout algorithm[35] which highlights the overall high density, and variation in connection
194   strengths across the cortex (**Figure 2d**).

195   *Interareal patterns of connectivity by output layer and class*
196   Network analysis of the ipsilateral intracortical connectivity matrix revealed a modular organization based
197   on the total output of a given cortical area. While this provides an important framework for understanding
198   macroscale rules of cortical connectivity, the contributions of distinct cell classes within each area to the
199   overall pattern are still unknown. To explore this, we first compiled groups of spatially-matched
200   experiments. These experiments were pulled from the 850 listed in **Figure 1a,** using up to 15 mouse lines
201   for coverage of layer/class within a given source. Each group was "anchored" by one of 90 Rbp4-
202   Cre_KL100 tracer experiments (green triangles, **Figure 1d**). Rbp4-Cre_KL100 is a L5 selective line which
203   labels all classes of projection neurons in L5. This line was chosen as the anchor because the largest
204   number of sources were injected (33 of 43 cortical areas had at least 1 experiment) of all the Cre lines.
205   Potential group members for each anchor were defined as experiments where the distance between the
206   Rbp4 and other experiment injection centroids was <500 μm. An experiment was only used once, even if
207   it was within 500 μm of two Rbp4 anchors. To be considered a complete group, at least one experiment
208   from a Cre line representing L2/3 IT, L4 IT, L5 IT, L5 PT, L6 CT, and a wild type or Emx1-IRES-Cre
209   dataset had to be present. Within a group, the median distance from the Rbp4-Cre_KL100 anchor was
210   296 μm. For some anchors, when a specific Cre line was otherwise missing, the injection centroid
211   distance exceeded 500 μm (range 502-616 μm, 24/332 total experiments). All experiments within a group
212   utilized the same tracer (*i.e.*, SypEGFP experiments were not grouped with EGFP experiments). In this
213   way, we identified 43 anchor groups composed of unique sets of experiments (n=364 total), representing
214   25 of 43 potential source areas (**Supplemental Table 3**).

215   The locations of all anchor groups and individual experiments are shown mapped onto the flat cortical
216   surface view in **Figure 3a**. Five examples are shown to illustrate layer selectivity, spatial matching of
217   injections into different lines, and cortical projection patterns by line, including sources from the prefrontal
218   cortex module (ACAd and MOs, **Figure 3b,c**), somatomotor module (SSp-m, **Figure 3d**), visual module
219   (VISp, **Figure 3e),** and medial module (VISam, **Figure 3f**). 2D overlays of the injection sites confirmed the
220   expected layer selectivity and relative size or proportion of cells labeled in these different experiments
221   (**Figure 3b'-f',** and see **Supplemental Figure 5** for individual panels). For example, prefrontal areas
222   ACAd and MOs are both agranular structures (lacking L4), and the corresponding injections into the
223   predominantly L4 IT Cre lines Scnn1a-Tg-3 or Nr5a1-Cre (colored in magenta) result in much sparser
224   labeling than for areas with a large L4, such as primary somatosensory and visual areas (compare **Figure**

225   **3b'-c'** with **d'-e'**). The distribution and density of cells labeled after viral infection of Cre-dependent
226   reporter in each injection also closely matches expectations based on ISH characterization of tdTomato
227   expression in Cre x Ai14 reporter lines for these regions[23] (http://connectivity.brain-map.org/transgenic).

228   From any given source, cortical projections labeled in the L5 Rbp4-Cre_KL100 line (middle column in
229   **Figure 3b-f**) appear to be more extensive than from any other line or layer. However, it is also visually
230   obvious that the projections labeled in different Cre lines originating from the same location had very
231   similar projection patterns overall (looking across rows). Indeed, it appears that the projections from every
232   other spatially-matched Cre line are a subset of the L5 outputs. Of note, the predominantly subcortical
233   projecting (see **Figure 1b**) L5 PT and L6 CT lines (3 columns on the right) also have varying amounts of
234   intracortical projections, which are still a subset of those mapped from L5 IT and pan Cre lines.

235   To quantitatively explore how similar, or different, cortical projection patterns are across cell classes from
236   the same location, we first manually curated the complete anchor group dataset (n=43 anchors, 364
237   experiments). This was accomplished by careful visual inspection of the corresponding high-resolution 2D
238   images for all possible cortical targets to identify true positive and true negative connections from each
239   experiment (43 ipsilateral and 43 contralateral targets, for a total of 31,304 connections manually
240   checked, data provided in **Supplemental Table 3**). We also noted when a target contained only fibers of
241   passage, and considered it as a true negative for subsequent binarization of the matrix. Using the output
242   of our automated segmentation and registration algorithms we generated multiple weighted connectivity
243   matrices, one for each Cre line, and applied the manually curated binary mask to remove all true negative
244   weights (*i.e.*, segmentation artifacts). As mentioned above, only 25 different cortical areas were
245   represented in the 43 anchor groups. This was due to both denser spatial sampling within a larger
246   structure (e.g. we targeted 6 retinotopic locations within primary visual cortex, 3 sub-regions in secondary
247   motor and 2 in the ventral part of anterior cingulate), and the replication of experiments in several visual
248   locations with the SypEGFP virus. To avoid biases related to differences between source areas, we
249   selected only one anchor group per cortical region, if there was a significant, positive correlation between
250   Rbp4-Cre_KL100 replicates (Spearman r >0.8). Following this selection, we present the results from 27
251   anchor groups, consisting of 25 unique areas and two locations in MOs and SSs. Eight of the lines
252   representing each layer/class with the most experiments in these 27 groups are shown in **Figure 4a**
253   (underlying data from these and the other 6 Cre lines provided in **Supplemental Table 3**). Of note, we
254   merged the data from C57BL/6J and Emx1-IRES-Cre experiments into one matrix, as these both account
255   for outputs of all projection neurons across layers in a cortical region. In support of this compilation, we
256   also found that cortical projection patterns between pairs of spatially-matched Emx1-IRES-Cre and wild
257   type experiments in 3 different regions were highly correlated, even given locations in opposite
258   hemispheres (Spearman r= 0.88 for VISp, 0.90 for VISl, and 0.97 for VISam, **Supplemental Figure 6**).

259   Overall, these matrices reveal several similar and unique features of projection neuron class-specific
260   connectivity between areas in terms of number, strength, and specificity of connections. First, we
261   quantified the number of output connections ("out-degree") for each experiment. Variation in out-degree
262   by source area in each line is shown in **Supplemental Figure 7a**. To assess for differences across lines,
263   we calculated the average out-degree in both hemispheres (**Figure 4b**). Overall, we find a significant
264   effect of both Cre line and hemisphere (but not the interaction) on the number of connections (2-way
265   ANOVA, p<0.0001). The mean numbers of C57BL/6J/Emx1-IRES-Cre connections are not significantly
266   different from Rbp4-Cre_KL100 or Tlx3-Cre_PL56 in either hemisphere, but are significantly higher than
267   all other Cre lines (Tukey's multiple comparison test, p<0.0001), except for Rorb-IRES-Cre on the
268   ipsilateral side. Similarly, Rbp4-Cre_KL100 also had significantly more connections on both ipsilateral and
269   contralateral hemispheres compared to every other line, except for Tlx3-Cre_PL56 on the contralateral
270   side. As also seen in the matrices, the L5 PT and L6 CT lines have the fewest number of connections to
271   regions in both hemispheres, followed by the L2/3, L4, and L5 IT lines. **Figure 4b** also shows that for
272   every line, there are fewer contralateral connections compared to ipsilateral connections.

6

273   **Figure 4a** and **b** show that L5 Rbp4-Cre_KL100 labeled cells project most widely, and are most like wild
274   type experiments for any given source. **Figure 3b-f** also shows that the connections from each line
275   appear to be a subset of the Rbp4-Cre_KL100 patterns, as opposed to a different set of target regions.
276   So, next we determined how much overlap there was between the specific targets contacted by each
277   experiment and the Rbp4 anchor within the spatially-matched groups (**Figure 4d**). C57BL/6J/Emx1-IRES-
278   Cre and Rbp4-Cre_KL100 shared, on average, 80% of the targets from any given source. A roughly
279   equal number of targets are unique to either Rbp4-Cre_KL100 or C57BL/6J/Emx1-IRES-Cre (12.7%, 7%)
280   which may be due to differences in sensitivities of the viral tracers, or the homozygosity of the Emx1-
281   IRES-Cre line. For every other Cre line, all target connections were a subset of the L5 Rbp4 targets
282   (**Figure 4c** white bars, <5% of the targets are unique to any Cre line). Together, it appears that L5 cells
283   project to almost all possible targets from any given source. Within L5, the L5 IT cells have the most
284   overlap with Rbp4-Cre_KL100 while L5 PT cells have more limited projections within the Rbp4 set, and
285   predominantly to the ipsilateral hemisphere (**Figure 3b-f and 4a**). L2/3 (and L4) IT cells project to a
286   subset of the same targets of L5. Fewer projections to the contralateral hemisphere appear to account for
287   most of the differences between L2/3 and L5 (**Figure 4b**), suggesting that most callosal projections arise
288   from L5 in the mouse.

289   Next, we looked at the strength of connections made by the projection neurons labeled in each line
290   (**Figure 4c**). After removal of the manually verified true negative connections, individual output strengths
291   still spanned ~5 orders of magnitude, like previously reported for both outputs and inputs in mouse and
292   macaque brains[4,36,37]. Projection strengths were positively correlated (r=0.43 to 0.89) between all pairs of
293   Cre lines from the same anchor group (**Supplemental Figure 8**)**.** Overall, we find a significant effect of
294   Cre line and hemisphere, and the interaction of these two factors, on the strength of connections (2-way
295   ANOVA, p<0.0001 for Cre line and hemisphere, p=0.02 interaction effect). Across all lines, the average
296   projection strengths are stronger within the ipsilateral compared to contralateral hemisphere (**Figure 4c**).
297   This overall pattern was also observed across individual sources within each line (**Supplemental Figure
298   7b**). The largest disparities in strength across hemispheres is seen in the L5 PT (blue) and L6 CT lines
299   (yellow). In other words, not only do these lines contact few targets contralaterally (<5, **Figure 4b**), but,
300   when axon terminals are present, they are ~1 order of magnitude weaker than the ipsilateral side
301   connections.

302   *Axon terminal lamination patterns and their relationship to source layer and cell class.*
303   L5 neurons make connections to essentially all the targets of that source area, and all other layers
304   contact a subset of these targets. Next, we looked at whether projection class-specific differences exist in
305   the targets at the level of layers.

306   First, we visually inspected and described the relative densities of axon terminal labeling across layers for
307   all targets in a subset of the Rbp4 anchor group experiments (79 of 364 experiments covering 14 source
308   areas in all 15 lines; total=6,794 connections checked for layer patterns, true negatives then removed).
309   Several frequently observed patterns emerged from this subset of representative experiments (**Figure 5a-
310   j**). The four most common lamination patterns include: (**a**) columnar, with relatively equal densities across
311   all layers (21%), (**b**) superficial and deep layers in equal densities (18%), (**c**) superficial layers only (25%),
312   or (**d**) deep layers only (18%). The remaining patterns observed (**e-j**) together account for 19% of all true
313   positive connections. Of note, almost all patterns involved dense terminals in L1, except for three rare
314   patterns (**e, i, j**; 2-4%), which were distinctive in that L1 contained relatively few labeled axons.

315   Following the qualitative assignment of axon terminals to a lamination pattern as shown, we checked
316   whether informatically-obtained values of projection strength by layer, derived following registration to the
317   Allen CCF, could quantitatively capture these patterns. The inset bars in **Figure 5a-j** show the average
318   fraction of the total projection volume per layer, scaled by the relative size of the layer in each target. We
319   used the actual ratio of each layer's volume per target for scaling because this number varies across
320   cortical areas (e.g. some areas have large L4, others very small). The resulting heat map in each panel
321   visually corresponded well to the qualitative classifications of laminar patterns.

7

322   We next performed unsupervised hierarchical clustering, for the *complete* dataset of **Figure 1a,** to
323   visualize laminar termination patterns from all source areas and Cre lines. In the heatmap shown in
324   **Figure 5k**, each column is a unique combination of mouse line, source area and target. Relative density
325   data were calculated as just described (*i.e.,* the fraction of the total projection in each layer, scaled by
326   relative layer size). Data included for clustering had to pass three filters. (1) target connection strength
327   (log10-transformed normalized projection volume) was greater than -1.5. This threshold was chosen
328   based on the frequency distributions for informatically-derived normalized projection volumes of the set of
329   manually-verified true positive and true negative connections (**Supplemental Figure 10**). At a log10
330   connection strength of -1.5, the number of true positives was first larger than true negatives. Less than
331   3% of true negative values remain, while over 50% of true positives are still present. (2) The percentage
332   of infection volume in the primary source was > 50%, and (3) self-to-self projections were removed.
333   Following these steps, if present, multiple experiments with the same source-line-target were averaged,
334   resulting in a total of 6,469 unique source-line-target connections in **Figure 5k**.

335   We performed unsupervised hierarchical clustering on the relative density of projections in L1, L2/3, L4,
336   L5, and L6a using Spearman rank correlations, and average linkages, to measure similarities. The first
337   dendrogram branch point split the targets based on the density of projections to L6a (low on the left, high
338   on the right). Then, within each of these two clusters, the next split was made by relative projection
339   density in L1. The third split was determined by L2/3 relative projection density. At this point, 6 clusters
340   were identified which resembled the manual categories, and we discuss each of these patterns further.
341   The median values for each layer and the overall frequencies of these clusters are shown in **Figure 5l,m**.
342   Clusters 1-3 had relatively weak projections to L6a compared to clusters 4-6. **(1)** Cluster 1 most
343   resembled the superficial layer pattern (**Figure 5c**), with dense projections in L1 and/or L2/3 (n=1,777,
344   27%). **(2)** Cluster 2 resembled the L1+L5 pattern (**Figure 5g**; n=314, 4.9%). **(3)** Cluster 3 resembled two
345   of the patterns avoiding L1 and L6 (**Figure 5e,j**, n=499, 7.7%), preferentially projecting into L2/3, L4 (if
346   present), and L5. Unlike clusters 1-3, clusters 4-6 had high projection density to L6a. **(4)** Cluster 4 was
347   the largest group (n=1,982, 31.0%) and most like the superficial and deep layer pattern (**Figure 5b**).
348   Cluster 4 is also likely to contain the targets with lamination patterns visually described as "columnar" and
349   "polylaminar" (**Figure 5a,f**), although even for those there does appear to be stronger projection density
350   to L1 and L6 (see insets in a,f). **(5)** Cluster 5 targets were most densely innervated in L2/3 and L6a, like
351   the pattern shown in **Figure 5i** (n=778, 12.0%). **(6)** Cluster 6 targets were most densely innervated in
352   deep layers like in **Figure 5d** (L5 and L6a, n=1,119, 17.3%). All 6 of these broad classes of lamination
353   patterns occurred in targets on the ipsi- and contra-lateral hemispheres at similar frequencies to the
354   overall ratio of the number of ipsi- and contra-lateral targets (68.77% ipsilateral, **Figure 5n**).

355   Next, we wanted to determine the relationships (if any) between these laminar patterns and the Cre lines
356   which label neurons of different layer-specific projection classes. For each mouse line, we calculated the
357   relative frequency of that line in each cluster, divided by the overall relative frequency of each Cre line in
358   the entire dataset. **Figure 5o** shows that the projections labeled in each mouse line have more than one
359   type of target layer pattern (*i.e.,* very few of the boxes are 0, or colored dark green). However, for most
360   lines, 1-3 layer patterns were identified that occur most frequently (pink-magenta). First, projections
361   labeled following tracer injections into C57BL/6J and Emx1-IRES-Cre mice, which label the outputs of all
362   layers and all classes together, are found with roughly equal frequencies in clusters 4,5, and 6 (all
363   involving dense targeting to L6). The two L2/3 IT lines, Cux2-IRES-Cre and Sepw1-Cre_NP39 are most
364   associated with cluster 3, as is one of the L4 IT lines, Nr5a1-Cre. In contrast, experiments from the other
365   two L4 IT lines, Rorb-IRES-Cre and Scnn1a-Tg3-Cre, which had some selectively for L5 as well as L4
366   (**Supplemental Figure 2**) occur with higher than expected frequencies in clusters 1 and 2. The L5 pan-
367   class line, Rbp4-Cre_KL100, is most associated with clusters 4 and 5, but the L5 IT line, Tlx3-Cre_PL56
368   is strongly associated with cluster 1. All four L5 PT lines were associated strongly with cluster 2, and three
369   of these were also identified at higher than expected frequencies in cluster 6 (A93-Tg1-Cre, Sim1-
370   Cre_KJ18, and Efr3a-Cre_NO108). The L5 PT line Chrna2-Cre_OE25, on the other hand, had relatively
371   more projections of the cluster 4 type. Finally, L6 CT lines, Ntsr1-Cre_GN220 and Syt6-Cre_KI148, were

372 like L5 PT lines in that they each had high relative frequencies of projections assigned to cluster 2 and 6
373 patterns.

374 The *most common* (but not all) laminar patterns from each Cre line are schematized in **Figure 5p**. In
375 summary, L2/3 and L4 (Nr5a1) source neurons project predominantly to the middle layers in a target
376 (L2/3, L4, and L5), avoiding L1. Other L4 source neurons project to L1 and either L2/3 or L5, avoiding L4
377 and L6. In L5, when both IT and PT classes are labeled, as in the Rbp4-Cre_KL100 line, projections
378 target L6 and *either* L1 or L2/3. L5 IT source neurons predominantly target superficial layers (L1 and
379 L2/3). L5 PT source neurons target either deep layers only (L5 and L6) or deep layers and L1, consistent
380 with the L5 Rbp4-patterns representing both IT and PT patterns. L6 CT source neurons project to L1 and
381 L5 or deep layers only.

Anatomical rules for determining hierarchical position in mouse isocortex.

383 Anatomical patterns of connections derived from anterograde and retrograde tracing data have been
384 used to describe the hierarchical relationships between cortical areas for decades[12,26,38,39]. In the
385 schemes based on the macaque monkey visual cortex, different lamination patterns correspond to
386 feedforward, feedback, and lateral connections between pairs of areas. Briefly, feedforward connections
387 were characterized by densest terminations in L4, feedback by the preferential avoidance of terminals in
388 L4, usually with denser projections in both superficial and deep layers, and lateral connections
389 characterized by having relatively equal density across all layers, including L4[12]. The fraction of
390 retrogradely labeled cells in supragranular layers has also been used as a continuous variable index of
391 hierarchical position in macaque cortex[39].

392 Here, we observed some obvious similarities between the previously published laminar patterns derived
393 from anterograde tracing data and our results, particularly for the feedback projection pattern. In our view,
394 clusters 2 and 4 projection patterns (most like **Figure 5g** and **Figure 5b**, respectively) are most like the
395 feedback rule described by Felleman and van Essen (1991). These patterns avoid L4, strongly targeting
396 L1 and either L5 or L6 and can arise from neurons in all layers and classes (**Figure 5o**). However, we did
397 not see a pattern emerge, either through unsupervised clustering or from the manual inspection, exactly
398 like the feedforward projection rule of Felleman and van Essen (*i.e.,* preferentially targeting L4). The most
399 similar projection pattern to a feedforward rule is seen in cluster 3 (most like **Figure 5e,j**), which involves
400 projections into L2/3, L4, and L5, arising most often from L2/3 and one L4 IT class (Nr5a1 only, **Figure
401 5o**). The sparsity of projections into L1 with denser signal in mid layers is consistent with an index of
402 feedforward connections recently described for mouse visual cortex[40], and suggests that cluster 5 may
403 also be a feedforward pattern in the mouse. Two patterns without an obvious match to previous literature
404 were the superficial layer only projections in cluster 1 and the deep layer-only projections in cluster 6.
405 Both patterns may be feedback because they do not involve mid-layers. Indeed, it was noted in Felleman
406 and van Essen (1991) that the superficial only pattern was occasionally seen, and they grouped them
407 with the feedback pattern because it did not involve L4. Also, of note, in the tracer experiments where all
408 projection neuron classes were labeled (C57BL/6J/Emx1-IRES-Cre) the most common patterns were 4,
409 5, and 6. Based on the above descriptions, these would also support the identification of both feedforward
410 (cluster 5) and feedback (cluster 4 and 6) types between areas when all neuron projection patterns
411 between a given source-target are compiled.

412 To determine whether the tentative assignments of layer patterns to feedforward or feedback connections
413 were consistent with past results and assumptions, we looked at specific pairs of connections where
414 hierarchical relationships have previously been explored or intuited in rodents. **Figure 6** shows two
415 examples of reciprocally connected pairs of areas within unimodal sensory regions (visual and
416 somatomosensory cortex) that are considered lower (primary) and higher (secondary) in a hierarchy. All
417 projections out of VISp to higher visual areas are generally described as feedforward, whereas the
418 reverse (to VISp from higher visual areas) are feedback[26,41–43]. We directly compared the axon projection
419 patterns originating from neurons in different layers and classes in these examples using the spatially
420 matched groups of experiments described in **Figures 3** and **4**. In the feedforward direction (VISp to VISal,

9

421 **Figure 6a**), projections from VISp terminated with different layer patterns depending on the Cre-defined
422 cells of origin. L2/3, L4, and L5 IT projections were densest in L2/3-L5 of VISal, and relatively sparse in
423 L1 and L6. These connections were assigned to cluster 3. Rbp4-Cre_KL100 projections from VISp to
424 VISal were densest in L2/3, L4 and L6, characteristic of cluster 5. The L5 PT and L6 CT cells projected to
425 L1 and L5 (cluster 2). In the opposite direction (VISal to VISp, **Figure 6a**), patterns were often different
426 from the corresponding reciprocal layer-specific projections. From VISal L2/3 IT cells, axons were
427 distributed across all layers, with a sparser region in L5 (cluster 4). There was also a weak projection from
428 L4 IT cells in VISal to VISp, with terminals in L1 and L5/6 (cluster 4). The projection originating from L5 IT
429 cells ended predominantly in superficial layers (cluster 1), while the Rbp4-Cre_KL100 labeled axons from
430 VISal to VISp were dense in L1 and deep layers (cluster 4). Again, projections from L5 PT and L6 CT
431 cells were sparse, but present in both L1 and L6 (cluster 4). Overall, more of the projections in the
432 feedforward direction involved middle layers, with sparser terminations in L1.

433 In the somatomotor module **(Figure 6b)**, we focused on projections between a primary (SSp-m) and
434 secondary (SSs) area as another example of a reciprocal feedforward (SSp-m to SSs) and feedback
435 (SSs to SSp-m) connection. Like for the visual pair, projections from L2/3 and L4 IT cells preferentially
436 innervated L2/3-L5, with relatively sparser terminals in L1 and L6. Both L5 IT and Rbp4-Cre_KL100
437 projections strongly innervate L1 and upper L5, unlike the VISp to VISal feedforward connection from L5
438 IT cells, which avoided L1. L5 PT and L6 CT cell projections were sparse, and to deep layers (cluster 6).
439 In the reverse direction (SSs to SSp-m), the patterns looked remarkably like the layer-specific feedback
440 projections from VISal to VISp. L2/3 IT cells terminated densely in mid layers (but appeared more diffuse
441 across the entire column), but the other lines containing IT cells all had similar projections to superficial
442 and deep layers. One very striking result from laying out the projection patterns originating from different
443 layers is in the Scnn1a-Tg3-Cre: L4 IT column. For both examples (visual and somatomotor), there is a
444 very strong connection originating from L4 cells in the lower area that preferentially terminates in mid-
445 layers of the higher area. This is clearly not the case in the reverse direction (higher to lower area). Two
446 additional examples of reciprocally connected areas within different modules (medial: RSPv to VISam and
447 prefrontal: ORBl to MOs) are shown in **Supplemental Figure 11**. These generally follow the same
448 patterns described above, including the obvious difference in strength and layer pattern in the L4 IT
449 projection between reversed directions.

450 We next looked at the layer-specific projection patterns between reciprocally connected areas assigned to
451 different network modules. The anterior cingulate cortex (ACA) exerts top-down control of sensory
452 processing in VISp[44,45]. We thus assume that the intermodule connection from VISp to ACAd is
453 feedforward, and ACAd to VISp is feedback (**Figure 7a**). In contrast to the intramodule feedforward
454 connections in **Figure 6** and **Supplemental Figure 11**, there is remarkable similarity in the target layer
455 patterns arising from L2/3, L4, and all classes of L5 cells. These all preferentially innervate L1 in ACAd
456 (cluster 1). In the feedback direction (ACAd to VISp), L2/3 cells also predominantly terminate in L1, but L5
457 cells project to both L1 and deep layers (L5 and L6, cluster 4), consistent with previous reports[44]. There
458 may also be a sub-layer distinction in these L1 terminals. Axons from VISp to ACAd seem to be relatively
459 deeper in L1 of ACAd, compared to the more superficial termination of ACAd axons in L1 of VISp. In
460 **Figure 7b**, we present images showing laminar termination patterns arising from the different cell
461 layer/classes between primary (MOp) and secondary (MOs) motor cortex, which we assigned here to the
462 somatomotor (MOp) and prefrontal (MOs) modules based on their overall connectivity strengths with the
463 other cortical areas. MOp is generally considered to be at a lower hierarchical level than MOs, although
464 MOp is also the final output of the cortex driving voluntary control of behavior. All the IT cells from MOp to
465 MOs appear to have more characteristics in common with intramodule feedforward connections
466 (superficial layers, with sparse terminations in L1), including labeled axons from the predominantly L4
467 line. From MOs to MOp, there is more involvement of L1 in all patterns, and the L5 IT pattern includes
468 deep and superficial layers like the Rbp4-Cre_KL100 experiment.

469 In summary, within a module, feedforward and feedback projections are consistent with the tentative
470 assignments to cluster/layer pattern described above. Feedforward projections have more target patterns

471 in clusters 3 and 5, feedback in clusters 2, 4 and 6. The relationship of cluster 1 to feedforward or
472 feedback is less clear in these intramodule examples, although results in **Supplemental Figure 11** would
473 support this pattern as feedforward, even with the L1 involvement. The intermodule connections from
474 ACAd to VISp further support characterization of the cluster 4 layer pattern (superficial and deep,
475 avoiding L4) as feedback, and, somewhat of a surprise, the cluster 1 pattern (superficial layers) as
476 feedforward. Also, in all cases, projections from L5 PT and L6 CT neurons, when present, appear to be of
477 the feedback type regardless of the overall top/down direction.

478 Taken together, these data suggest that the assignment of "feedforward" and "feedback" to specific
479 connections between any pair of areas should account for all the contributions from each source layer,
480 and the overall mix of target lamination patterns for a given connection (see also **Supplemental Figure
481 12** showing this concept, with more detail below).

482 Based on the anatomical analyses as described, we grouped the observed target layer patterns into
483 either feedforward (clusters 1,3,5) or feedback (clusters 2,4,6) (**Figure 8a**). Quantification of the relative
484 frequency of these patterns for intra- and inter-module connections showed that clusters 1 and 4 occurred
485 more often than expected in intermodule connections; clusters 3, 5, and 6 were identified more often in
486 intramodule connections (**Figure 8b**), consistent with data in **Figure 6** and **Figure 7**. All source modules
487 had relatively high frequencies of the feedforward pattern described by cluster 3 for their intramodule
488 connections (**Figure 8c**). Between modules (**Figure 8d**), visual, temporal, and somatomotor were strongly
489 associated with the superficial lamination pattern of cluster 1, which we classified as feedforward.
490 Prefrontal connections were relatively more frequently assigned to cluster 4 (feedback), and all other
491 modules occurred more often than expected in cluster 5 (feedforward).

492 *Unsupervised hierarchy of all cortical areas from layer termination patterns*
493 We next determined whether it was possible to use the layer termination patterns from the layer-specific
494 projection neuron classes defined by the Cre lines to define a direction of information processing
495 throughout ipsilateral cortex. We defined hierarchical position for a cortical source area as the number of
496 feedback connections originating from this area minus the number of feedforward connections, divided by
497 their sum. Each connection was also normalized by a confidence level for the Cre line in providing
498 information about the direction (see equations 1 and 2 in the methods). Similarly, the position in the
499 hierarchy as a target is the normalized number of feedforward minus feedback connections terminating in
500 the target. Each of these measures is bounded between -1 to 1. We used the sum of these measures as
501 the hierarchical position (see equation 3 in the methods, possible range then becomes -2 to 2). Individual
502 pair-wise measures for each connection, based on the clustering assignments to target lamination pattern
503 types, are shown in **Supplemental Figure 12.** This matrix represents the concept of a "multigraph", in
504 that there are many possible edges between two nodes (e.g. each of the 13 Cre lines), and all information
505 is used when searching for the optimal hierarchical positions. We searched over all possible mappings
506 between the layer pattern type (the 6 clusters above) and feedforward and feedback assignments, and
507 checked the self-consistency for every assignment. For the whole cortex assignment, the highest self-
508 consistency (see equation 4 in methods) was obtained when clusters 1,3 and 5 were assigned to one
509 type, and 2, 4 and 6 to the opposite. These are the *same* classifications derived from the above
510 anatomical analyses, providing an example of how the human brain is an excellent unsupervised
511 hierarchy discoverer.

512 Hierarchical positions of 37 (of the 43 parcellated) cortical areas are presented in **Figure 8e** (AUDv, GU,
513 PERI, and ECT did not have data that passed thresholding; VISC and SSp-un were additionally removed
514 for having only n=2 connections from 1 Cre line). By this measure, primary visual cortex (VISp) is at the
515 bottom and the dorsal part of anterior cingulate cortex (ACAd) at the top. Areas were color coded by
516 module assignment, which reveals a general pattern for prefrontal areas (red) to be higher in the
517 hierarchy, and unimodal sensory regions (VISp, SSp, AUDp) to be closer to the bottom. For the entire
518 cortex, the global hierarchy score (see equation 4 in methods) is 0.128 (range 0 to 1). Therefore, while we
519 find a global hierarchy, there are still many connections for which a hierarchical organization may not

520   provide a full explanation. We performed the same analyses on intramodule connections separately.
521   Here, we observed a hierarchy score of 0.51 for the temporal, 0.33 for the visual module, 0.31 for
522   anterolateral, 0.12 for medial, 0.09 for somatomotor, and 0.03 for prefrontal, given the same pattern
523   assignments to feedforward (1,3,5) or feedback (2,4,6). The range in values suggests that different
524   schemes, or different assignments of connections to feedforward and feedback, may better describe
525   organization of connectivity within different modules. We also determined the relative order of all 10 visual
526   areas, which span two modules here (visual and medial, colored blue and purple, respectively). Previous
527   analyses based on tracer experiments in the mouse have mapped these areas into ventral and dorsal
528   streams[46]. A representation of their hierarchical positions overlaid onto a weighted network diagram is
529   shown in **Figure 8h** (dorsal stream areas on the right, ventral on the left of the circle). The edge weights
530   in the network diagram are derived from the matrix of **Figure 2b**, and nodes are ordered from bottom to
531   top (VISp, VISl, VISpl, VISrl, VISal, VISli, VISa, VISpm, VISpor, and VISam).

532   *Hierarchy of cortical network modules*
533   We also determined the overall "feedback-ness" of each module's ipsilateral outputs (as opposed to the
534   individual nodes/areas) by measuring the number of feedback minus feedforward patterns, divided by
535   their sum for every module as a source to all other modules (**Figure 8f**). Then, we calculated the
536   difference between these feedback fractions for every pair of modules in both directions to obtain a single
537   measure (the intermodule hierarchy index) predicting the forward/back relationship between each pair
538   (**Figure 8g**). From this plot, it is obvious that the prefrontal module is above all other modules (e.g., every
539   circle plotted for prefrontal as a source on the y-axis is positive on the x-axis). Conversely, the
540   somatomotor module is below all other modules. We thus anchored the hierarchy at the top and bottom
541   with prefrontal and somatomotor modules. **Figure 8i** shows a network diagram with each module
542   collapsed into a single node. Edges are the sum of all the weights between modules from **Figure 2b**. The
543   modules were positioned from top to bottom based on the data points in **Figure 8g**. Remarkably, the
544   order is self-consistent at all levels given the available data. We did not have enough data or connections
545   between anterolateral and medial, and anterolateral and visual modules to confirm these positions,
546   however these are also the weakest of the intermodule connections (thinnest lines in **Figure 8i**). The
547   combination of layer/class-specific projection patterns between network modules thus enabled the
548   prediction of a consistent hierarchical framework for cortical information processing, with three modules
549   containing primary sensory regions at the bottom (somatomotor, temporal, and visual), progressing to
550   higher levels with modules containing more associational areas (medial, anterolateral) and ending in the
551   prefrontal cortex.

552   Discussion
553   Here we used a genetic tracing approach, building on our previously established viral tracing, whole brain
554   imaging, and informatics pipeline, to map projections originating from unique cell populations in the same
555   cortical area. Two key features of our high-throughput connectivity mapping pipeline are the automated
556   segmentation of fluorescent signal, from which we calculate measures of long-distance projection
557   strength between areas, and the registration of every experiment to our fully annotated 3D mouse brain
558   reference atlas, the Allen CCF. Jointly, these methods enabled a comprehensive yet detailed view of
559   mesoscale cortical wiring patterns, and the derivation of several general anatomical rules of long-range
560   intracortical connections. Specifically, we show: (1) network analysis of intracortical connectivity patterns
561   reveals a modular organization of cortical areas, (2) L5 neurons in any given source area make the most
562   connections, and neurons in L2/3, L4, and L6 project to a subset of these L5 targets, (3) intracortical
563   target lamination patterns are diverse, but at a coarse-grained level are related to layer of origin and are
564   like previously described anatomical rules for defining feedforward/feedback connections, (4) projections
565   originating from specific source layers/classes and target layer patterns together can define a single
566   direction of information flow (*i.e.,* a hierarchy) between cortical areas and between network modules, with
567   primary sensory areas and related modules at the bottom, and prefrontal areas at the top.

568   Our previously generated whole brain mesoscopic connectome provided a comprehensive, directed, and
569   quantitative connectivity map between areas of the mouse cortex[4]. In the current study, we used these
570   data and a novel voxel-based model[31] to provide a macroscale organizational framework for viewing
571   cortical areas as networks of connections. Through community detection analysis of the ipsilateral
572   intracortical connectome, we identified six modules. The **first** module ("prefrontal") consisted of cortical
573   areas in predominantly frontal, agranular regions strikingly similar to those recently proposed as the
574   mouse prefrontal cortex[47]. Very broadly, the function of the prefrontal cortex is cognition, and it is likely
575   that the connections into and out of this module enable the necessary information flow for incoming
576   sensory and behavioral state input that influence voluntary control of behavior. Indeed, there is relatively
577   strong output from this module to primary motor cortex (MOp, **Figure 2b**), and strong input to secondary
578   motor cortex (MOs) from many regions in other modules. The **second** module ("anterolateral") included
579   all three agranular insular subregions, plus gustatory and visceral cortex, consistent with a role for insular
580   cortex in integration of taste and body homeostasis/energy needs[48,49]. At lower levels of spatial resolution
581   ($\gamma<1$) these areas were part of a larger sensory module together with our **third** module ("somatomotor").
582   The somatomotor module contained all the primary somatosensory regions, secondary somatosensory
583   cortex, and MOp. All SSp divisions project to SSs and MOp, and to MOs, which is in the prefrontal
584   module. Although the MOp is not sub-parcellated in the Allen CCF, our projection mapping data show that
585   projection domains are preserved in MOp when originating from the different SSp domains (*i.e.,* there are
586   specific terminal fields in MOp for barrel field, trunk, lower limb, upper limb, nose, mouth), as previously
587   reported[3]. The **fourth** module ("visual") contained primary visual cortex and six out of nine higher order
588   visual areas. The remaining three visual areas (VISa, VISam, and VISpm) were grouped with the three
589   retrosplenial cortex subregions (RSPagl, RSPd, RSPv) into the **fifth** module ("medial"). At lower spatial
590   resolution, these two modules (visual and medial) consistently merged into one, reflecting the high
591   connectivity strengths between all visual areas. However, the medial module areas are more strongly
592   connected to prefrontal areas (particularly ACAd, ACAv, and ORBvl). The **sixth** module ("temporal")
593   contained both auditory sensory regions (AUDp, AUDd, AUDv, AUDpo) and associational cortical areas,
594   perirhinal (PERI), ectorhinal (ECT), and temporal association cortex (TEa). This combination is the least
595   intuitive of all these modules, and may be a consequence of limitations in the underlying dataset.
596   Specifically, in only one experiment did we successfully label projections from ECT cortex (shown in
597   bottom right panel, **Figure 2a**), and so the voxel-based model had very little information to use for
598   prediction of connection strengths[31].

599   Within these modules and areas, we identified generalizable layer-specific intracortical projection
600   patterns. For a given cortical source area, L2/3, L4, L5 PT, and L6 CT cells project to a subset of the
601   target regions contacted by L5 neurons. Notably, all the excitatory neuron classes we surveyed had
602   intracortical projections labeled outside of the infection area, including the L4 IT and subcortical PT and
603   CT projection neurons. This somewhat unexpected result could be caused by Cre lines with less than
604   perfect specificity. However, we also found that when long-distance projections are present from PT or CT
605   cells, they have distinct termination patterns compared to the IT lines. These projection patterns were
606   consistent with characteristics of feedback pathways, even in connections that were overall feedforward.
607   A feedback collateral arising from deep layer subcortical-projection neurons may thus be another
608   generalizable feature of PT and CT intracortical axons[50].

609   The strength and presence of projections between areas from the predominantly L4 Cre lines was also
610   unexpected. Canonical circuits, mostly derived from primate and cat, do not include inter-areal L4
611   excitatory neuron projections[51]. The three Cre lines used here had varying degrees of selectivity for L4
612   expression (**Supplemental Figure 2**), with some expression in L5 for both the Scnn1a-Tg3-Cre and
613   Rorb-IRES-Cre lines. These two Cre lines also contain cells classified into both L4 and L5a types based
614   on transcriptomics; while the Nr5a1-Cre line appears most specific to L4 cell types[15]. Thus, it is difficult to
615   definitively conclude that these inter-areal projections originate from L4 rather than L5. Differences in the
616   number of connections and the specificity of these inter-areal connections suggest that if the origin is in
617   L5, they are at least a unique subclass of projection neurons. It is also worth noting that although the

13

618 prefrontal and some other areas in the cortex are considered "agranular", *i.e.,* lacking a distinct L4, Cre
619 expression is often still detectable, though much sparser, in the so-called L4 lines used here.

620 Classic definitions for PT and CT cell classes exclude contralateral cortical projections[20], roughly
621 consistent with our observations. However, our data also showed that for some source areas, particularly
622 in the prefrontal module, PT and CT lines had labeled axons that crossed the callosum, terminating in a
623 small number of contralateral cortical targets. Overall, most callosal projections were made by neurons in
624 L5, and, to a lesser extent, L2/3 and L4 Cre lines, consistent with expectations from previous results[52].
625 The number of ipsilateral connections made by L2/3 IT cells was similar to L5 IT cells; however, there
626 were significantly fewer connections on the contralateral side. A recent analysis of the rat macroscale
627 cortical connectome identified a set of general rules regarding ipsilateral (associational) and contralateral
628 (commissural) connections that are mostly consistent with our observations; namely that all cortical areas
629 have more associational than commissural targets[8]. The mesoscale connectome data we present here
630 reveals that some of these differences can be better explained at the level of cell class.

631 Cortical areas are densely interconnected, and projections arise from all layers. Here, we first present an
632 organizational scheme, the network, that groups cortical areas based on the strength of their connections.
633 This kind of network view of cortical organization presents a structural view of all possible paths of
634 information flow between areas and modules, but does not impose a direction or order on that flow.
635 Another very influential organization scheme is the cortical hierarchy. The existence of a hierarchy implies
636 classifying inter-areal connection types into at least two general classes: feedforward or feedback. From
637 the macaque brain, studies have demonstrated that specific anatomical projection patterns between
638 areas are characteristic of either a feedforward or feedback connection[12,13]. These primate rules were
639 applied to build the visual cortex hierarchy that has inspired multiple computational models of cortical
640 function[12]. Several models assign feedforward connections for information processing, and feedback
641 connections as carrying a learning signal[14,53]. Another popular model for cortical computations is
642 predictive coding[54], in which feedforward connections represent an error signal, while feedback
643 connections represent predictions, and local circuits integrate them[55].

644 Partial hierarchies of the visual cortex exist for rodents, also based on anatomical projection patterns from
645 anterograde tracing studies[26,40,56]. Differences between those patterns used in the primate were noted,
646 and re-classified for rodent. Specifically, feedforward connections were characterized by having less
647 dense axon terminations in L1 compared to L2/3, but axon terminals still spanned L2/3 to L5 evenly[40].
648 Feedback avoided L4 (like for the primate), terminating most densely in L1 and L6. We noted the same
649 kinds of patterns in visual cortex feedforward and feedback connections. Whether these patterns can be
650 extended to other sensory, motor, and associational modules (including those with "agranular" cortex[57])
651 was less clear from previous studies. Our analysis within and between modules suggests that there are
652 several patterns associated with feedforward and feedback connections, but that every pattern can be
653 classified into one or the other type. Within most modules, feedforward has the characteristics described
654 above (i.e., densest in L2/3-L5), but between modules the feedforward connections were either dense in
655 L2/3 and L6, or preferentially terminated in superficial layers (L1-L2/3). Feedback patterns matched
656 previous descriptions in that there was preferential termination in L1 + deep layers (L5 or L6), or deep
657 layers only. One of the most unusual patterns, not reported previously to the best of our knowledge, that
658 clearly differentiated known feedforward from feedback connections was the strong presence of axons
659 originating from L4 and ending in L2/3-L5. This occurred only in the feedforward direction of reciprocally
660 connected pairs, but in the reverse direction there was both fewer axons from L4 and, when present, they
661 were associated with more feedback patterns (avoiding L4). We also observed a striking relationship
662 between feedforward/feedback patterns with the cell layer/classes, namely, supragranular (L2/3 and
663 upper 4) neurons have predominantly feedforward projections, whereas infragranular (L5 and L6)
664 neurons have both feedforward and feedback projections. However, as we have already noted, these
665 types and their relationship to cell classes are also dependent on the specific connection.

14

666   Using these rules for feedforward and feedback across all cortical areas, we observe that the global
667   organization of cortical connections is consistent with a hierarchy, in which a bottom-to-top direction can
668   be defined. However, we want to emphasize that the hierarchical position does not explain all the
669   connections, as the pathways between cortical areas are complex. The model used for **Figure 8e** shows
670   an optimized hierarchy, but it is not the only possible solution, akin to the differences described for
671   determining hierarchical order in primate visual cortex using the fraction of supragranular projection
672   neurons (SLN), instead of discrete levels as in the Felleman and Van Essen diagram[12,39].

673   Given the number of different connection types arising from a single area, we believe that new
674   computational models, containing more than feedforward and feedback connections between nodes, are
675   needed. This may be especially true when moving beyond models of sensory processing in the cortex.
676   We would like to emphasize and encourage the adoption of a multigraph view of connectivity, in which
677   two areas can be connected by multiple edges; each edge having an associated weight, type and
678   subtype. We challenge the theoretical community to expand computational algorithms beyond those
679   focused on classical graph structure. Additional data types that could predict directionality in cortical
680   organization may also be added to these connections in the future. For example, the ratios of specific
681   interneuron types, systematically mapped across all cortical areas, has recently been related to
682   hierarchical position in the mouse[58].

683   The expansion of the Allen Mouse Brain Connectivity Atlas to include mapping of projections from
684   genetically-identified cell classes represents a big step toward a true *meso*scale connectome. Here, we
685   present the addition of ~ 1,000 new experiments to our online resource (http://connectivity.brain-
686   map.org/), but focus only on the analysis of intracortical projection data. However, the complete brain-
687   wide projection patterns are also already available for interested researchers to pursue a multitude of
688   questions and analyses, and new results incorporating subcortical inputs and outputs may alter our view
689   of a hierarchy in interesting and important ways. Finally, one of the limitations inherent in the population-
690   based mapping approach used here is that we are still missing information at a more fine-grained level of
691   cell types. Recent efforts and future work will undoubtedly further subdivide these broad classes of
692   pyramidal neurons, at the level of areas as well as layers and projections, into specific cell types using
693   morphology, physiology, and transcriptomics[15,17]. Here, we focused only on broad classes to derive
694   general patterns of mesoscale cortical connectivity, which will be instructive and informative for future
695   connectome data from more refined cell types. However, future large-scale efforts aimed at mapping the
696   projections of specific cell types rather than classes, and even single cells[59,60] will no doubt reveal
697   additional principles of cell type-specific connectivity across the brain, moving us even closer to a full
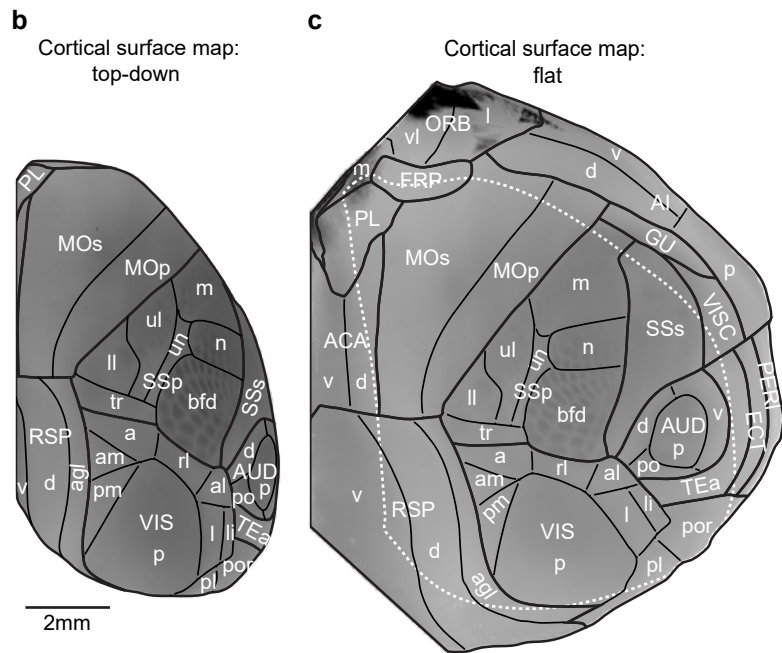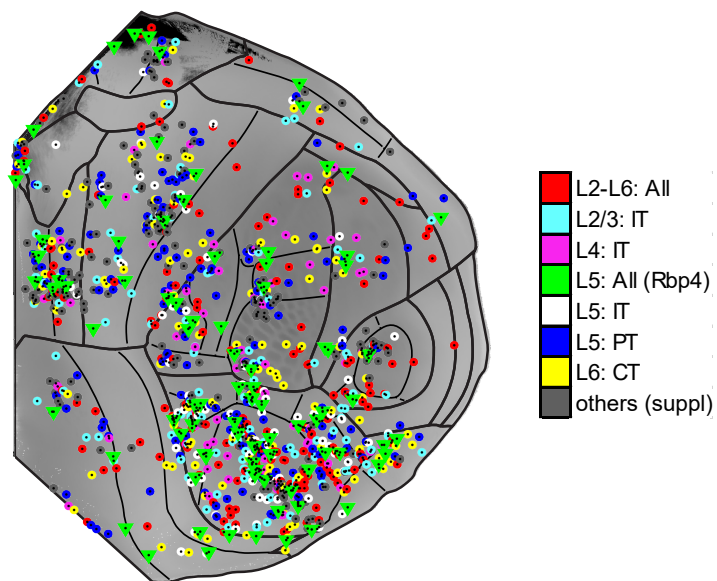698   mesoscale connectome.

699

700   Figures

701

702

Figure 1

a

Mouse Line	C57BL/6J	Emx1-IRES-Cre	Cux2-IRES-Cre	Sepw1-Cre_NP39	Nr5a1-Cre	Scnn1a-Tg3-Cre	Rorb-IRES2-Cre	Rbp4-Cre_KL100	Tlx3-Cre_PL56	A93-Tg1-Cre	Chrna2-Cre_OE25	Efr3a-Cre_NO108	Sim1-Cre_KJ18	Ntsr1-Cre_GN220	Syt6-Cre_KI148	TOTAL
Layer	L2-6	L2-6	L2/3	L2/3	L4	L4/5	L4/5	L5	L5	L5	L5	L5	L5	L6	L6	
Projection Class	IT PT CT	IT PT CT	IT	IT	IT	IT	IT	IT PT CT	IT	PT	PT	PT	PT	CT	CT	TOTAL
prefrontal FRP	1		1												1	3
MOs	9		9	3	2		2	9	9	5	4	5	12	6	8	83
ACAd	3	5	2			2		3	2	3	2	2		3	3	30
ACAv	2		4	1		2		3		2	2	2		2	3	23
PL	1	1	3					1	1	1				1		9
ILA	1		1					1		1	2			1	1	8
ORBl	4		1	1	1				1	1	1				1	12
ORBm	1	1	2					1							2	7
ORBvl	2		1					3	1		1					8
anterolateral GU								1	1							2
VISC	4												1			5
AId	2		3					1	1		1			1	1	10
AIp			1					1		1	1					4
AIv								1								1
somatomotor MOp	8		1		1	1		1	1	2	2	1	3	2	3	26
SSp-n	3			1	1	1	1	2		1	1	1			2	15
SSp-bfd	6	1	4	1	2	3	1	3	2	2	1	2	2	8	2	40
SSp-ll	3		3		1		2	3	3	2		1	1	2	1	22
SSp-m	5		2		2	4	1	2	1	1		1	2	3	2	26
SSp-ul	2		2			2		2	1	1	1	1	2			14
SSp-tr	2							1	1	1	1	1	1			8
SSp-un														1		1
SSs	3		3		1	1	1	4	2	2	2	1	2	2		25
visual VISal	1	1	2			2		3	3	3				2		17
VISl	4	6	7		1		2	2	5	4		3		4	1	39
VISp	31	26	23	2	7	10	4	17	20	24	5	3	2	16	4	194
VISpl								1	2	2				1	2	8
VISli	2		1		1			2	1	2				1	1	11
VISpor	2	1	5			1		4	2	2				4	3	24
VISrl		2	3		2	1		3	3	2			1		1	18
medial VISa				1				1	1	3		1		2		9
VISam	3	2	5			1		2	6	1		1	1	3	1	26
VISpm	1	4	2			3	2	3	3	1	1			2	1	23
RSPagl	1	2	3					3	2	2				5	1	19
RSPd	2	2	1			1		2	2	1		1		4		16
RSPv	3	3	4	1		2		3		5	3	1			3	28
temporal AUDd	2		1	1	1			1								6
AUDp	4	2	2			1	1	1	1				1	2	1	16
AUDpo	1	3	3					1		1				1		10
AUDv	1															1
TEa												1		1		2
PERI																0
ECT	1															1
Sources	35	16	31	9	13	17	10	33	26	29	19	18	14	27	25	
Expts	122	62	105	12	23	38	17	90	78	77	34	29	31	81	51	850

b Cortical surface map: top-down

2mm

c Cortical surface map: flat

d Centroid locations of all experiments (n=1,082)

- L2-L6: All (red)
- L2/3: IT (cyan)
- L4: IT (magenta)
- L5: All (Rbp4) (green)
- L5: IT (white)
- L5: PT (blue)
- L6: CT (yellow)
- others (suppl) (gray)

703   **Figure 1. Systematic generation of cortical projection mapping data by area and mouse line. (a)**
704   Location and number of 850 tracer injection experiments across cortical areas and selected mouse lines.
705   These 15 lines (C57BL/6J through Syt6-Cre_KI148) were used most extensively across cortical regions
706   to map projections using Cre driver lines with expression preferentially in the layers and projection neuron
707   classes indicated **(b)** Mouse isocortex is parcellated into 43 areas in the Allen CCF. The positions of most
708   areas are visible in our standard top-down view of the right hemisphere cortical surface. This view is
709   obtained by projecting the maximum density voxels from the average template brain, used to construct
710   the CCF, along a curved coordinate system meant to match the columnar structure of the cortex (as
711   opposed to a direct z-projection). **(c)** Areas that occupy very lateral, frontal and midline positions are
712   better viewed in a flattened map of the mouse cortex. The flatmap is generated by constructing a 3D-to-
713   2D mapping such that the 2D Euclidean distance of every point on the flatmap to a pair of anchor points
714   are the same as their 3D geodesic distance (shortest path along surface), resulting in the coordinate
715   along one axis formed by the anchor points. This process is repeated for a second pair of anchor points
716   to form the second axis. The white dotted line indicates the boundaries of what is visible in the top-down
717   view in **b**. **(d)** The positions of all 1,082 injection centroids are plotted on the flat cortical surface. The 850
718   experiments are color coded as indicated by layer-specific projection class. The remaining 232 are shown
719   in dark gray.

720

Figure 2
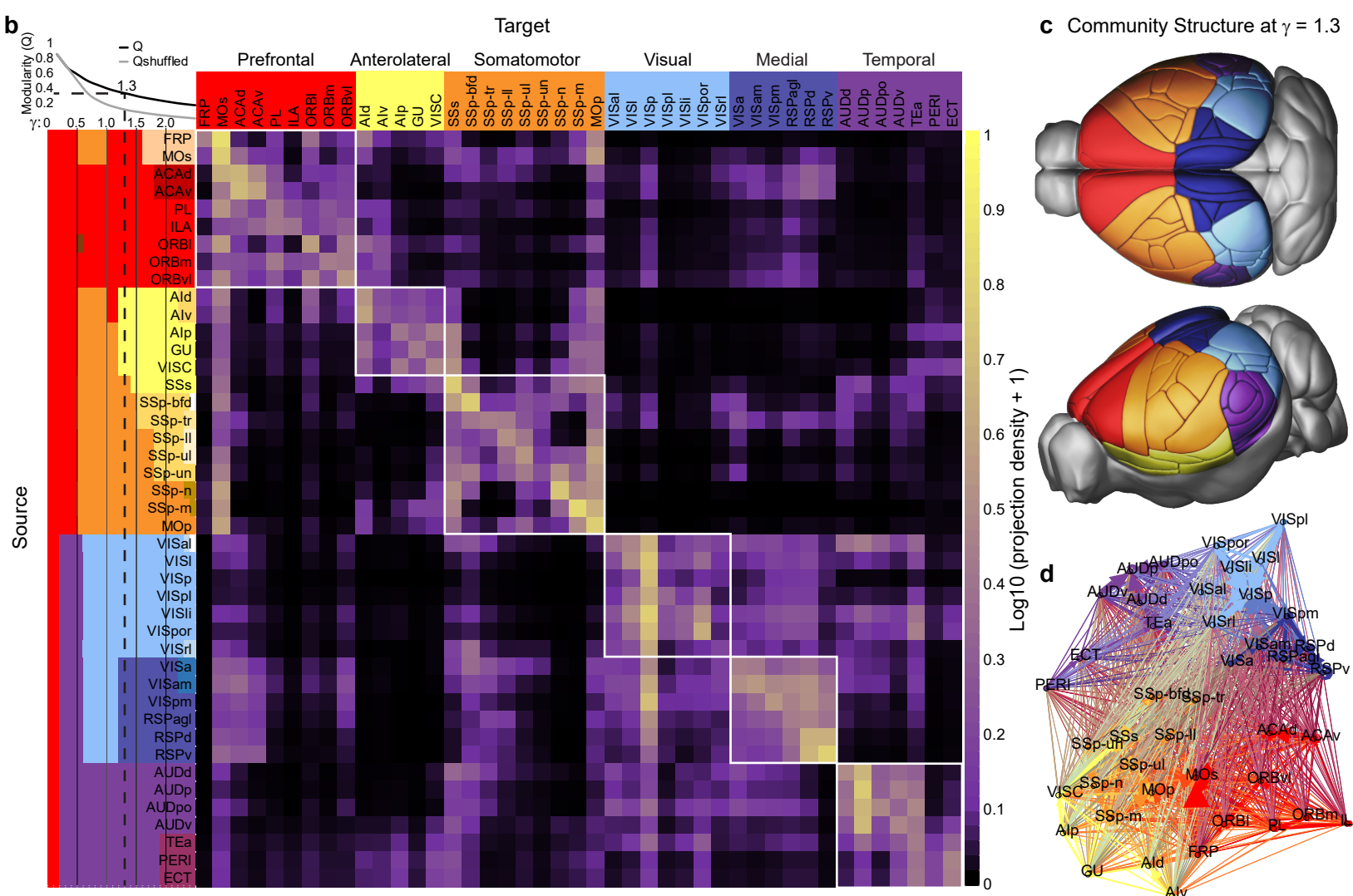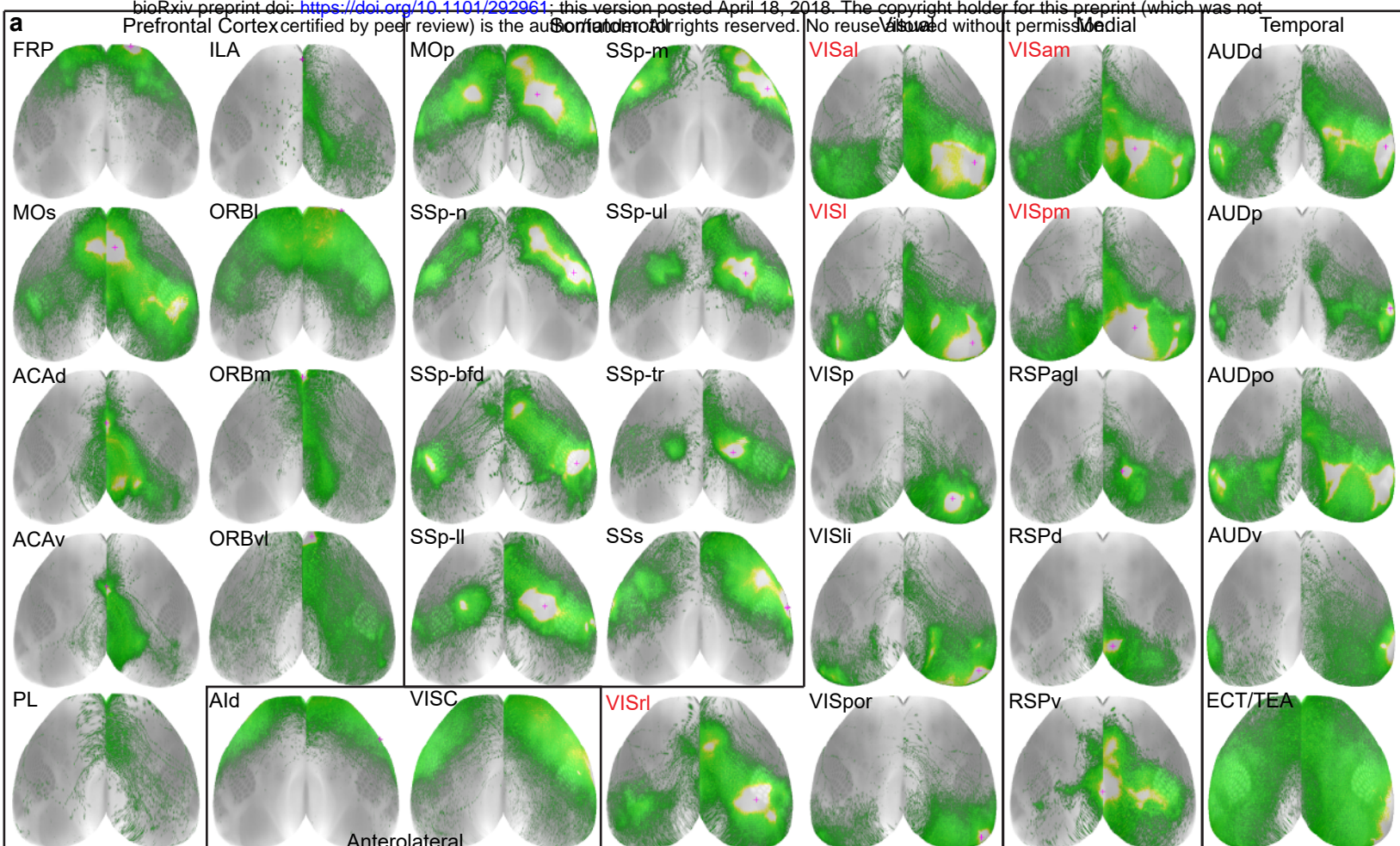
721 **Figure 2. Modular organization of intracortical projection patterns based on the wild type**
722 **connectivity matrix**. **(a)** Top down cortical surface views showing the relative projection densities of
723 labeled axons (normalized within each experiment, white is saturation) originating from 35 cortical source
724 areas in C57BL/6J (black labels) or Emx1-IRES-Cre (red labels) mice. Red cross hairs indicate the
725 location of the injection centroid. Some are not visible in the top down view. **(b)** Weighted connectivity
726 matrix for 43 cortical areas. The data matrix was derived from the voxel-based model of Knox et al., 2018
727 and shows the connection strength as log10-transformed normalized projection density (the sum of
728 predicted density per voxel in a target region normalized to that target's volume). Rows are sources,
729 columns are targets. Cortical areas are ordered first by module membership then by ontology order in the
730 Allen CCF. Colors along the matrix axes indicate community structure with varying levels of resolution (γ =
731 0-2.5 on the y axis, γ = 1.3 only on the x-axis). The modularity metric (Q) is plotted for each level of γ,
732 along with the Q value for a shuffled network containing the same weights. Community structure was
733 determined independently for each value of γ, but colors were matched to show how communities split as
734 the resolution parameter is increased. **(c)** Cortical regions color-coded by their community affiliation at γ =
735 1.3 show spatial relationships. **(d)** Diagram shows the ipsilateral cortical network in 2D using a force-
736 directed layout algorithm. Nodes are color coded by module. Edge thickness shows relative projection
737 density and edges between modules are colored as a blend of the module colors.

738

Figure 3.
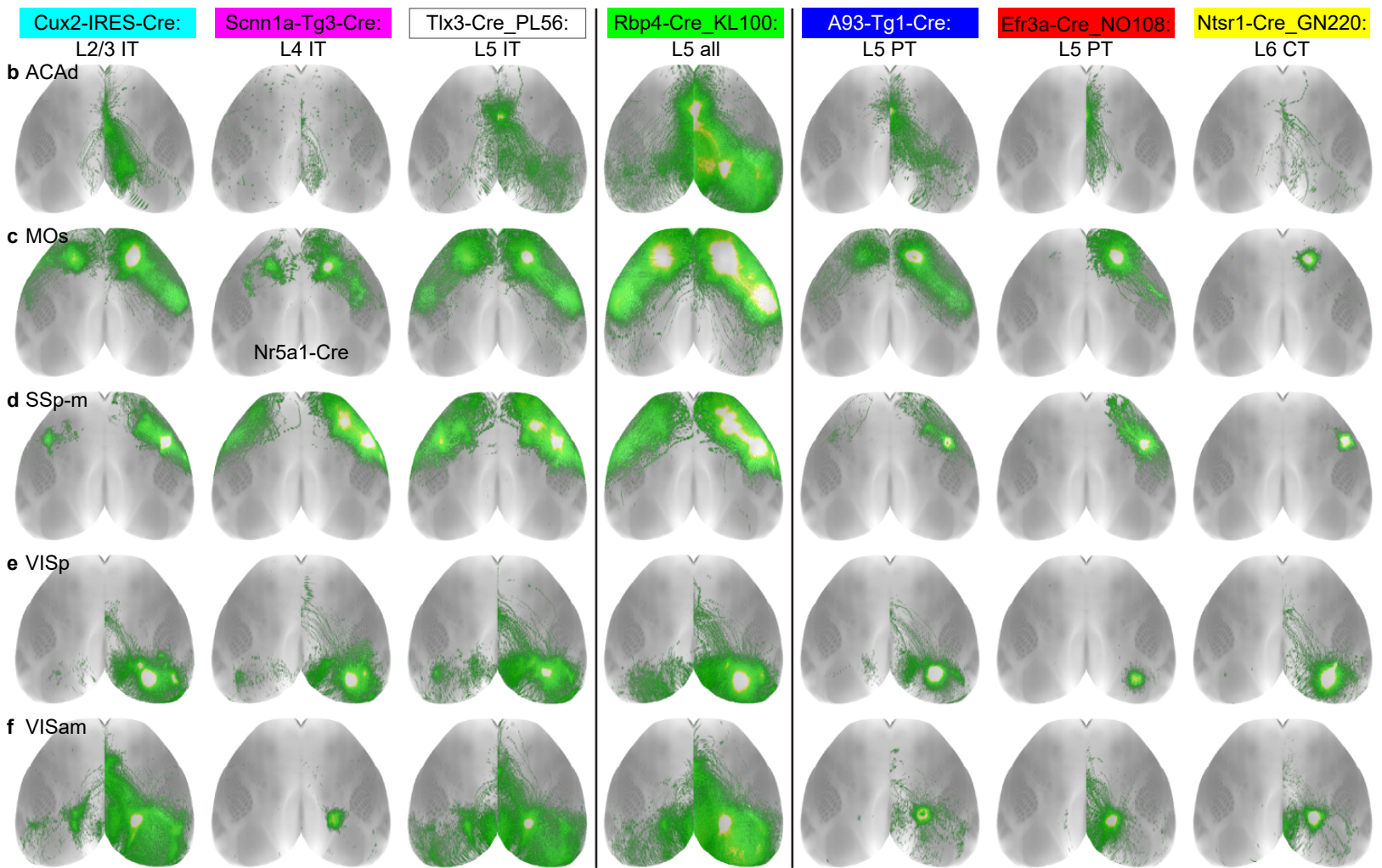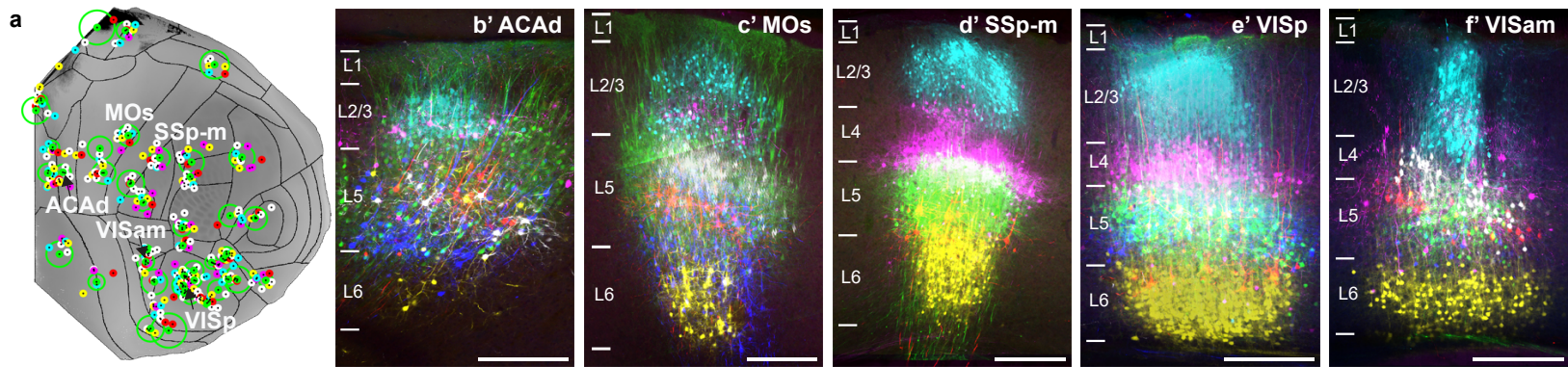
739   **Figure 3. Comparison of layer- and class-selective intracortical projection patterns. (a)** 43 groups of
740   spatially-matched experiments to an Rbp4-Cre_KL100 anchor were collated based on having a
741   "complete" membership roster; representing L2/3 IT, L4 IT, L5 IT, L5 PT, L6 CT and the L5 IT PT CT data
742   from Rbp4-Cre_KL100. Each Rbp4-Cre experiment is shown as a green dot; all other experiments are
743   color coded by layer and class as indicated. The green circle indicates the variance in distance to Rbp4
744   for each group. The five labeled groups are the examples shown in **b-f** (ACAd, MOs, SSp-m, VISp, and
745   VISam). **(b'-f')** 2-photon images acquired at the center of each injection site were manually overlaid by
746   finding the best match between the top of L1 (pial surface) and bottom of L6 (white matter boundary)
747   between each experiment, and then pseudocolored by Cre line to highlight the layer selectivity of Cre
748   expression. Scale bar = 250 μm. **(b-f)** Top down views of the labeled axonal projections across the cortex
749   originating from the infected neurons shown in **b'-f'**. Three Cre lines that label IT projection classes in
750   L2/3 (Cux2-IRES-Cre), L4 (Scnn1a-Tg3-Cre, or Nr5a1-Cre as indicated for MOs) and L5 (Tlx3-Cre_PL56)
751   are shown to the left of Rbp4-Cre_KL100. Three lines that predominantly label PT or CT projection
752   neurons in L5 (A93-Tg1-Cre, Efr3a-Cre_NO108) and L6 (Ntsr1-Cre_GN220) are shown to the right.
753   These lines also have intracortical projections, but target a smaller number of areas.
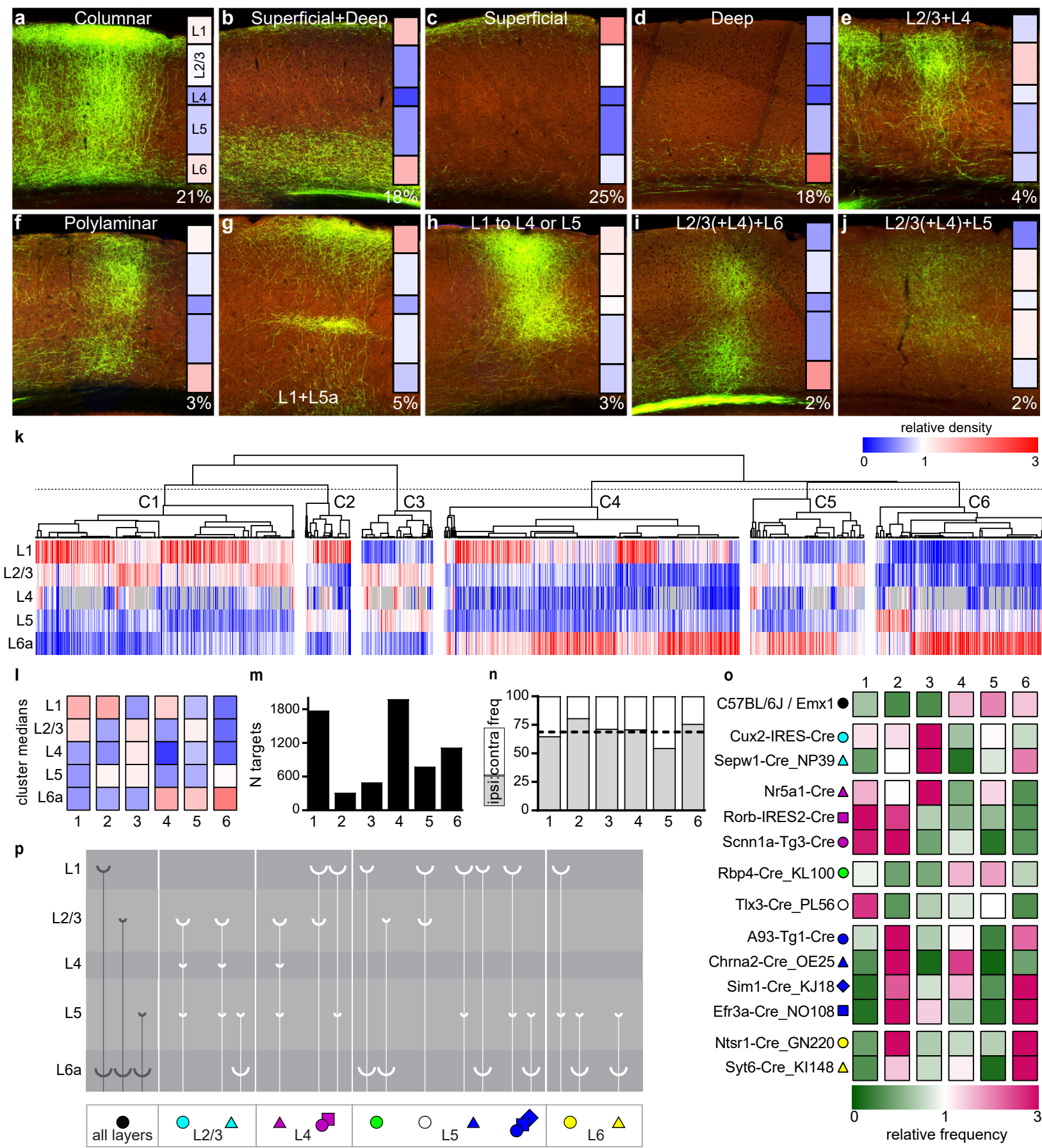
754

19
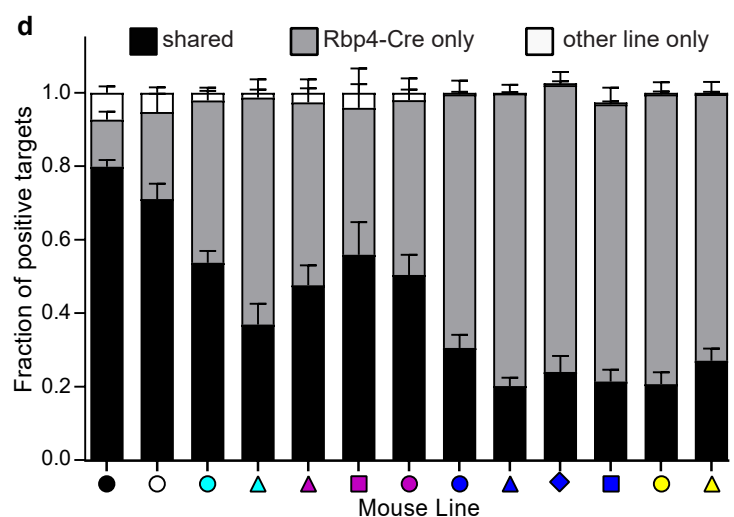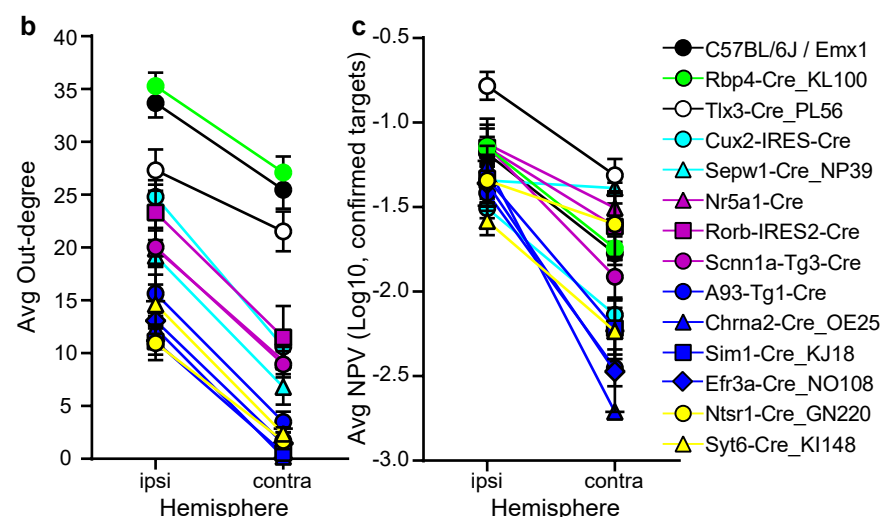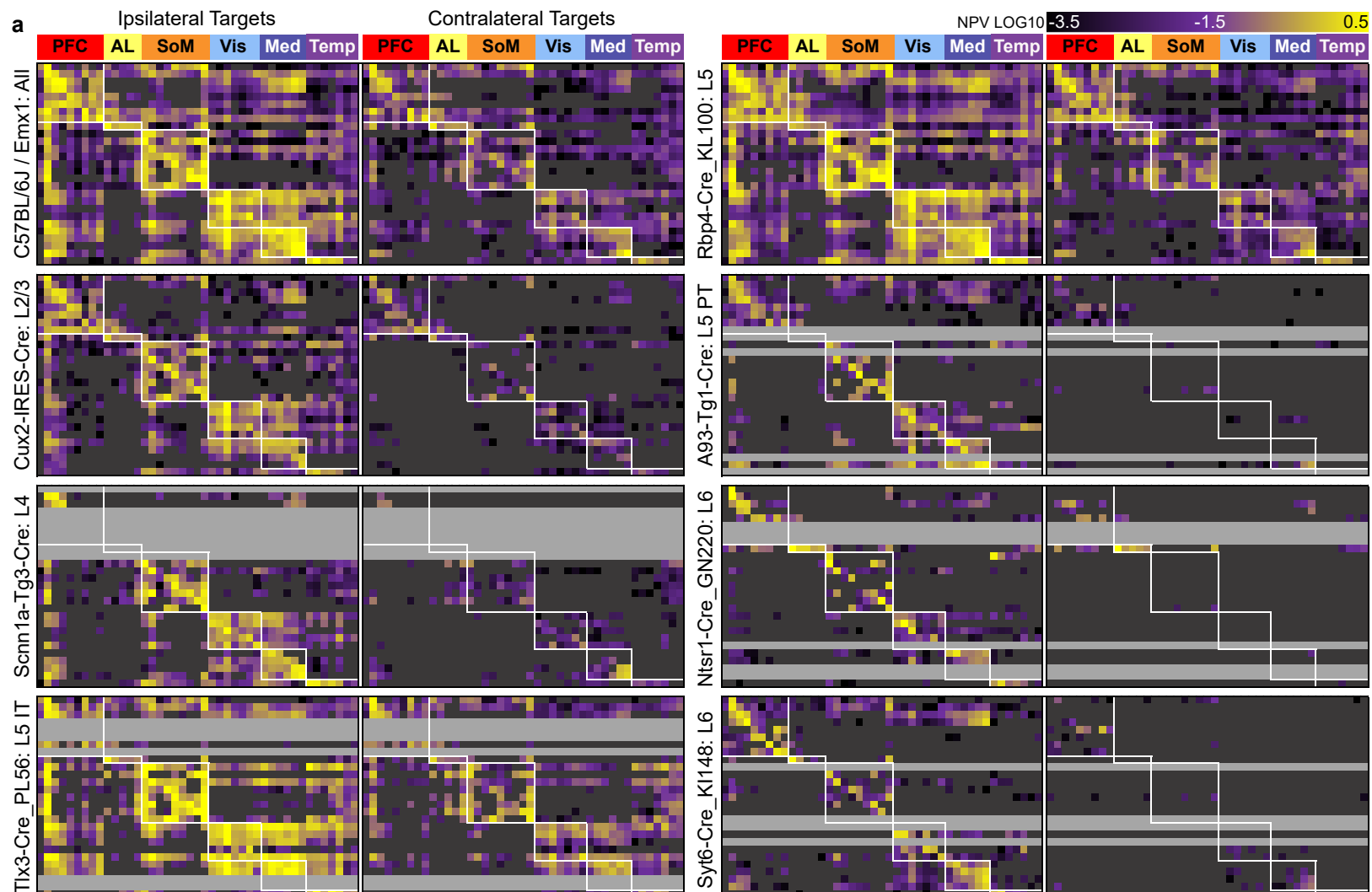
Figure 4

755 **Figure 4. Cre line and layer-specific cortical outputs. (a)** Eight directed, weighted, connectivity
756 matrices (27 x 86) are shown for mouse lines representing projections labeled from different layers and
757 cell classes. Each row of one matrix contains experimental data from one of 27 unique source areas.
758 Columns show the 43 ipsilateral and 43 contralateral cortical target regions. Rows and columns follow the
759 same module-based ordering in each matrix. Areas and connections belonging to the modules assigned
760 using the ipsilateral voxel-based model data in Figure 2b are indicated by the white boxes. For every
761 experiment, each of the 43 ipsilateral and 43 contralateral targets were inspected and assigned as
762 containing either true positive or true negative axon terminal labeling. All true negatives (including passing
763 fibers) were masked and colored dark grey. Rows for which an experiment was not completed are light
764 grey. This was often because of low levels of Cre expression in those areas. The color map corresponds
765 to log10-transformed normalized projection volumes in each target (range $10^{-3.5}$ to $10^{0.5}$, truncated at both
766 ends). **(b)** The average out-degree across all sources represented in each matrix for each Cre line is
767 plotted for the ipsilateral and contralateral cortex. **(c)** The average strength of all the connections (log10-
768 transformed normalized projection volume) across source areas in each matrix are plotted for ipsilateral
769 and contralateral hemisphere by Cre line. **(d)** Binary present or absent calls for the targets of each
770 experiment were compared to the presence/absence calls from the matched Rbp4-Cre_KL100 anchor
771 experiment. The average fraction of true positive targets shared by each line with its Rbp4 anchor
772 experiment is plotted in the bar graph (black) as well as the average fraction of positive targets that are
773 unique to Rbp4 (gray) or unique to the line indicated (white). Symbols or bars in **b-d** show mean +/- SEM.
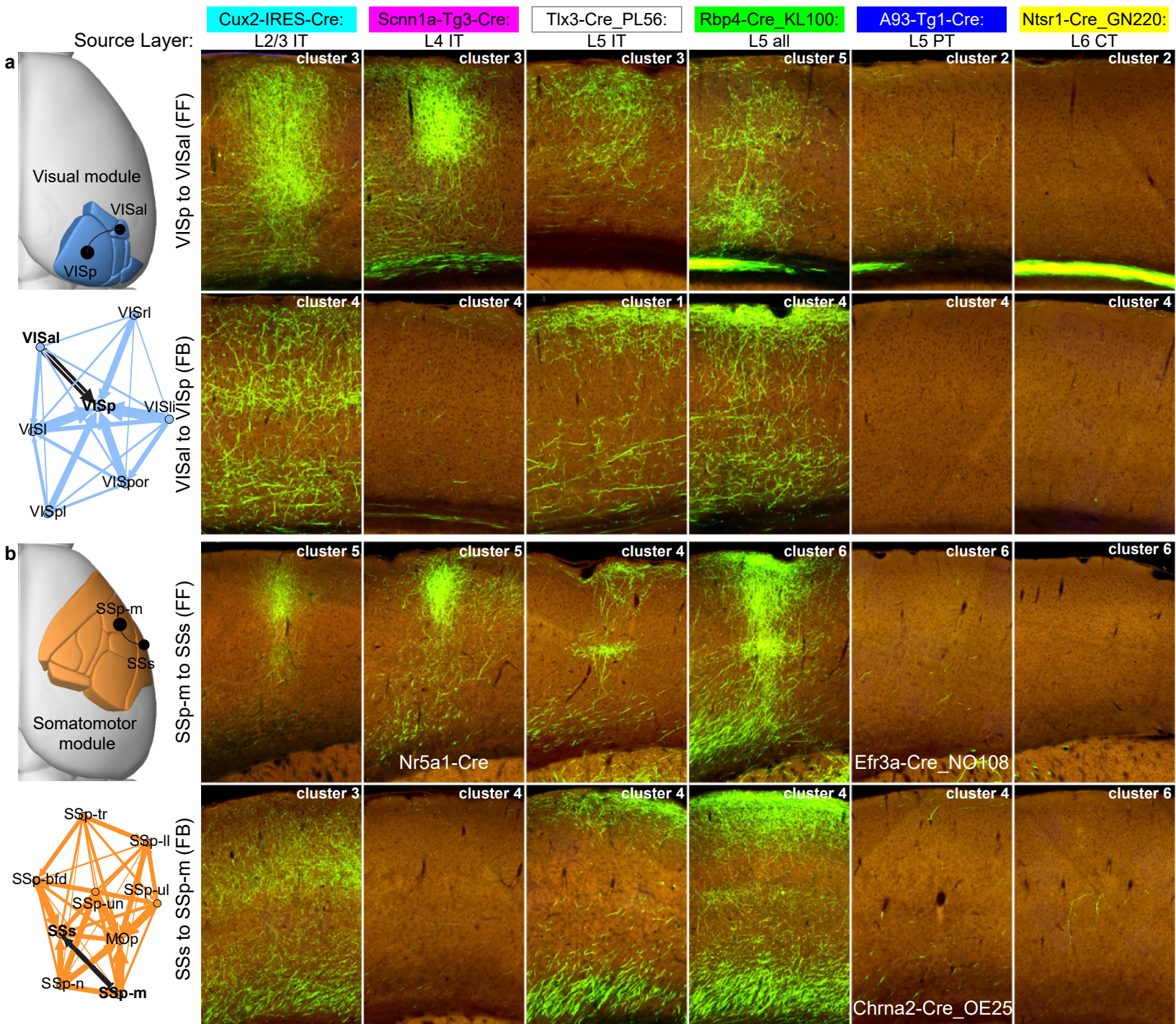
774

Figure 5

a Columnar 21%
b Superficial+Deep 18%
c Superficial 25%
d Deep 18%
e L2/3+L4 4%

L1
L2/3
L4
L5
L6

f Polylaminar 3%
g L1+L5a 5%
h L1 to L4 or L5 3%
i L2/3(+L4)+L6 2%
j L2/3(+L4)+L5 2%

relative density
0   1   3

k

C1   C2   C3   C4   C5   C6

L1
L2/3
L4
L5
L6a

l cluster medians
L1
L2/3
L4
L5
L6a
1 2 3 4 5 6

m N targets
1800
600
1 2 3 4 5 6

n ipsi:contra freq
100
75
50
25
1 2 3 4 5 6

o

	1	2	3	4	5	6
C57BL/6J / Emx1 ●						
Cux2-IRES-Cre ○						
Sepw1-Cre_NP39 △						
Nr5a1-Cre ▲						
Rorb-IRES2-Cre ■						
Scnn1a-Tg3-Cre ●						
Rbp4-Cre_KL100 ●						
Tlx3-Cre_PL56 ○						
A93-Tg1-Cre ●						
Chrna2-Cre_OE25 ▲						
Sim1-Cre_KJ18 ◆						
Efr3a-Cre_NO108 ■						
Ntsr1-Cre_GN220 ○						
Syt6-Cre_KI148 △						

relative frequency
0   1   3

p

L1
L2/3
L4
L5
L6a

all layers ●   L2/3 ○ △   L4 ▲ ■   ● ○ L5 ▲ ◆ ■   L6 ○ △

775 **Figure 5: Diverse target lamination patterns in mouse cortex. (a-j)** Relative densities of axon terminal
776 labeling across layers for every cortical target were visually inspected for a subset of experiments, and
777 then classified into one of ten categories based on overall observations. Four patterns occurred most
778 frequently; **(a)** columnar, with relatively equal densities across all layers (21%), **(b)** superficial and deep
779 layers in equal densities (18%), **(c)** superficial layers only (25%), or **(d)** deep layers only (18%). Additional
780 patterns of note, although rare (<10%), included those in which L1 received relatively few axons **(e, i, j)**.
781 Insets show the results of averaging informatically-derived quantification of relative layer density (the
782 fraction of the total projection signal in each layer, scaled by the relative layer volumes) for all targets
783 manually classified to that category. A relative density value of "1" (color = white) indicates that the
784 fraction of axon labeling within a specific layer is equal to the relative size of that layer in that target, *i.e.,* it
785 is neither more nor less dense than expected if axons were distributed evenly across layers, given
786 differences in layer volumes. Values <1 indicate lower than expected density and >1 higher than
787 expected density. Relative densities were color coded from 0 (blue) to 1 (white) to 3 (red). The color map
788 key applies for panels a-l. **(k)** Unsupervised hierarchical clustering using spearman correlation and
789 average linkages on the relative density values per layer. Each column is a unique combination of cre
790 line, source area and target, after thresholding as described in the results. The dotted line indicates where
791 the dendrogram was cut into 6 clusters. **(l)** Median relative density values by layer for each of 6 clusters.
792 **(m)** Total number of targets in each cluster. **(n)** The frequency of ipsilateral and contralateral targets
793 assigned to each cluster. The dotted line indicates the overall frequency of ipsilateral targets (68.77%).
794 **(o)** The relative frequency of each Cre line appearing in one of the 6 clusters. The fraction of experiments
795 in a cluster belonging to each Cre line was divided by the overall frequency of experiments from that Cre
796 line in the complete dataset. A relative frequency value of "1" (color = white) indicates that Cre line
797 appeared in that cluster with the same frequency as in the entire dataset. Values <1 (green) indicate
798 lower than expected frequency, and >1 (pink) indicate higher than expected frequency of that Cre line in a
799 cluster. **(p)** Schematic diagram showing the relationships between the layer and class of origin in the
800 source area (Cre line symbols at the bottom) with the most frequent axon lamination patterns observed in
801 the target area.

802

Figure 6

Source Layer:

Cux2-IRES-Cre: L2/3 IT | Scnn1a-Tg3-Cre: L4 IT | Tlx3-Cre_PL56: L5 IT | Rbp4-Cre_KL100: L5 all | A93-Tg1-Cre: L5 PT | Ntsr1-Cre_GN220: L6 CT

a Visual module

VISp to VISal (FF): cluster 3, cluster 3, cluster 3, cluster 5, cluster 2, cluster 2

VISal to VISp (FB): cluster 4, cluster 4, cluster 1, cluster 4, cluster 4, cluster 4

b Somatomotor module

SSp-m to SSs (FF): cluster 5, cluster 5, cluster 4, cluster 6, cluster 6, cluster 6

Nr5a1-Cre, Efr3a-Cre_NO108

SSs to SSp-m (FB): cluster 3, cluster 4, cluster 4, cluster 4, cluster 4, cluster 6

Chrna2-Cre_OE25

803 **Figure 6. Intra-module projection patterns between reciprocally connected areas originating from**
804 **different layers/classes. (a)** In the visual module, VISp and VISal are reciprocally connected (black and
805 white arrows). VISp is the de facto bottom of visual cortex hierarchies. The output to VISal from VISp is
806 feedforward (FF). The reciprocal connection (VISal to VISp) is feedback (FB). **(b)** In the somatomotor
807 module, the primary somatosensory cortex (SSp), like VISp, is the de facto bottom of the hierarchy. SSp-
808 m sends feedforward projections to the secondary somatosensory region (SSs). SSs sends feedback
809 projections to SSp-m. Modules from Figure 2b are shown spatially mapped on the cortex and as a force-
810 directed network layout with the thickness of the lines corresponding to relative connection weights. 2P
811 images in the approximate center of the axon termination fields for each target region show the laminar
812 distribution of axons arising from labeled neurons in the different Cre lines, as indicated. Images were
813 rotated so that the pial surface is always at the top of each panel. The cluster assignment for that line-
814 source-target combination (columns **in Figure 5k**) is also indicated in each panel. One very striking
815 difference between FF and FB connections was the strength and pattern of projections originating from
816 L4 IT cells (second column). L4 IT cells in both modules strongly projected to the target in the FF
817 direction, with patterns showing sparser axons in L1. In the FB direction, the L4 projection was weaker
818 and ended in L1.

819

Figure 7

Source Layer:

Cux2-IRES-Cre: L2/3 IT — Scnn1a-Tg3-Cre: L4 IT — Tlx3-Cre_PL56: L5 IT — Rbp4-Cre_KL100: L5 all — A93-Tg1-Cre: L5 PT — Ntsr1-Cre_GN220: L6 CT

a — VISp to ACAd (FF); ACAd to VISp (FB)

b — MOp to MOs; MOs to MOp

Syt6-Cre_KI148

820 **Figure 7. Inter-module projection patterns between reciprocally connected areas originating from**
821 **different layers/classes. (a)** Many reciprocal connections exist between areas in prefrontal and visual
822 modules, e.g. VISp and ACAd. ACAd exerts top-down control of VISp activity, so we assume this
823 connection is FB, and that the reverse is FF. **(b)** Reciprocal connections also exist between nodes of the
824 prefrontal and somatomotor modules, e.g. MOs and MOp. Modules from Figure 2b are shown spatially
825 mapped on the cortex and as a force-directed network layout with the thickness of the lines
826 corresponding to relative connection weights. Like in Figure 6, 2P images in the approximate center of the
827 axon termination fields for each target region show the laminar distribution of axons arising from labeled
828 neurons in the different Cre lines, as indicated. Images were rotated so that the pial surface is always at
829 the top of each panel. The cluster assignment for that line-source-target combination (columns **in Figure**
830 **5k**) is also indicated in each panel.

831

Figure 8
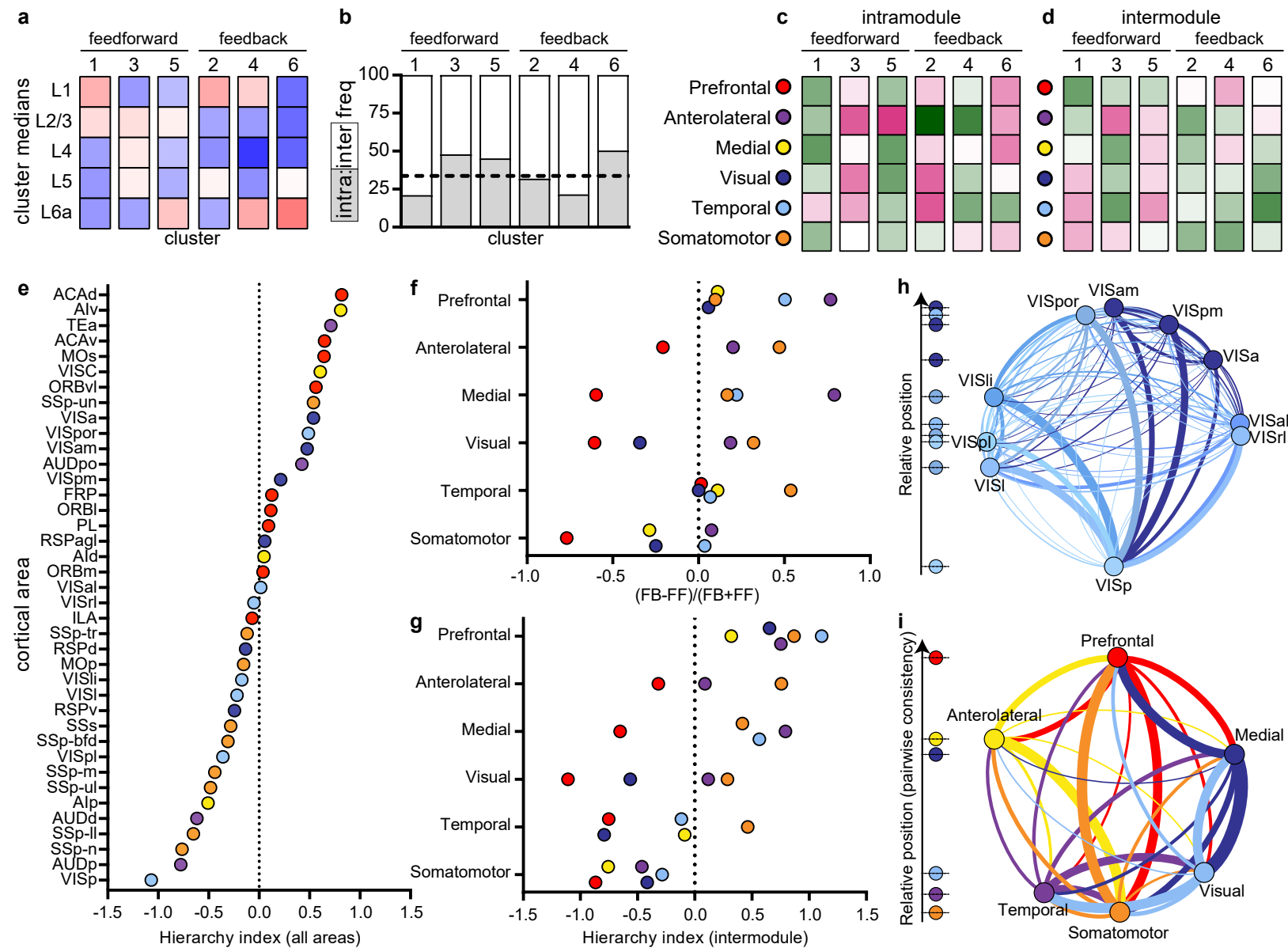
832   **Figure 8. Organization of network modules into a hierarchy based on anatomical patterns of**
833   **connections. (a)** The six layer patterns identified through clustering in **Figure 5k** were classified as either
834   feedforward or feedback. Clusters 1,3, and 5 were considered as characteristic of different feedforward
835   projections. Clusters 2,4, and 6 were considered characteristic of different feedback projections. **(b)** The
836   relative frequency of inter-module and intra-module connections is plotted for each cluster. The dotted
837   line indicates the overall frequency of intramodule connections (33.74%). The laminar patterns of clusters
838   1 and 4 were relatively more frequent in intermodule connections, while clusters 3, 5, and 6 were
839   associated more with intramodule connections. The relative frequencies within clusters are shown for
840   each of the six modules as sources, for intramodule **(c)** and intermodule connections **(d)**. **(e)** 37 cortical
841   areas are rank ordered by their hierarchical index scores and color coded by module assignment. **(f)** The
842   relative differences in feedback to feedforward patterns between modules. Source module is indicated on
843   the y-axis, and the relative differences in patterns between that module and every other target module is
844   represented by the colored circles. Modules which had <10 connections were removed from analyses.
845   Positive values indicate more feedback (FB) than feedforward (FF) connections from the source (y-axis)
846   to target (plotted circles) module. Negative values indicate more FF than FB connection types. **(g)** The
847   difference between the values plotted in (f) for each pair of modules as source and target, used to
848   determine pairwise hierarchical positions. Positive values indicate the overall direction is feedback, given
849   the reciprocal connection, from the source module on the y-axis to the target module (circles). Negative
850   values indicate a feedforward connection from source to target modules. All intermodule connections from
851   the prefrontal cortex were feedback. All from the somatomotor module were feedforward. Thus, these two
852   modules formed the top and bottom of an intermodule hierarchy. **(h)** Network diagram showing
853   interconnections of all 10 visual areas (visual module = blue, medial module = purple). Edge width
854   indicates relative connection strength (from **Figure 2b**). The direction of the curved line shows outputs
855   (clockwise) and inputs (counter-clockwise) from each node. Nodes are positioned along a circle perimeter
856   based on hierarchical score, with VISp at the bottom and VISam at the top. All areas have strong
857   feedback to VISp. **(i)** The intermodule network diagram shows each module as a node, with edge
858   thicknesses based on the sum of connection weights from **Figure 2b**. Based on the pair-wise calls from
859   data in **(g)**, we propose a hierarchical order of network modules that is consistent across levels. At the
860   bottom is somatomotor, temporal, and visual, then medial, anterolateral, and, at the top, prefrontal.

861

24

862 ## Acknowledgements

872

873 ## Author Contributions

874 Conceptualization: H.Z., J.A.H., S.M. Supervision: H.Z., J.A.H., S.M., A.B., L.N., N.G., P.A.G., J.L., S.A.S,
875 J.W.P., A.J., C.K. Project administration: S.M., S.W.O., W.W. Investigation, validation, methodology and
876 formal analyses: J.A.H., S.M., K.E.H., J.D.W, J.K., P.B., S.C., L.C., A.C., N.G., N.G., C.G., P.A.G.,
877 A.M.H., A.H., R.H., L.K., J.L., J.L., M.T.M., M.N., L.N., B.O., S.A.S., Q.W., A.W, H.Z. Data curation:
878 J.A.H., K.E.H., J.D.W., P.B., S.C., A.H., B.O., W.W. Visualization: J.A.H., K.E.H., J.D.W., L.N., D.F., S.M.,
879 M.N. The original draft was written by J.A.H., with input from K.E.H., J.D.W, S.M., Q.W., P.A.G., C.K., and
880 H.Z. All co-authors reviewed the manuscript.

881 ## Methods

882 ### *Mice*

883 Experiments involving mice were approved by the Institutional Animal Care and Use Committees of the
884 Allen Institute for Brain Science in accordance with NIH guidelines. Sources of mouse lines are listed in
885 Supplemental Table 1. Characterization of the expression patterns of Cre driver lines used in this study
886 have previously been described [23]. Links to image series data are available through the Transgenic
887 Characterization data portal (http://connectivity.brain-map.org/transgenic). Cre lines were derived on
888 various backgrounds, but the majority were crossed to C57BL/6J mice and maintained as heterozygous
889 lines upon arrival. Tracer injections were performed in male and female mice at an average age of P56 +
890 10 days. Mice were group-housed in a 12-hour light/dark cycle. Food and water were provided ad libitum.

891 ### *Tracers and injection methods*

892 rAAV was used as an anterograde tracer. For most regions, stereotaxic coordinates were used to identify
893 the appropriate location for a tracer injection[61]. For a subset of experiments in the left hemisphere, we first
894 functionally mapped the visual cortex using intrinsic signal imaging (ISI) through the skull, described
895 below. A pan-neuronal AAV expressing EGFP (rAAV2/1.hSynapsin.EGFP.WPRE.bGH, Penn Vector
896 Core, AV-1-PV1696, Addgene ID 105539) was used for injections into wildtype C57BL/6J mice (stock no.
897 00064, The Jackson Laboratory). To label genetically-defined populations of neurons, we used either a
898 Cre-dependent AAV vector that robustly expresses EGFP within the cytoplasm of Cre-expressing infected
899 neurons (AAV2/1.pCAG.FLEX.EGFP.WPRE.bGH, Penn Vector Core, AV-1-ALL854, Addgene ID 51502).
900 or, a Cre-dependent AAV virus expressing a synaptophysin-EGFP fusion protein to more specifically label
901 presynaptic terminals (AAV2/1.pCAG.FLEX.sypEGFP.WPRE.bGH, Penn Vector Core).

902 Functional mapping of visual field space by intrinsic signal optical imaging (ISI) was used in some cases
903 to guide injection placement. Additional details of this procedure can be found online (http://help.brain-
904 map.org/display/mouseconnectivity/Documentation?preview=/2818171/10813533/Connectivity_Overview.
905 pdf). Briefly, a custom 3D-printed headframe was attached to the skull, centered at 3.1 mm lateral and 1.3
906 mm anterior to lambda on the left hemisphere. A transcranial window was made by securing a 7-mm
907 glass coverslip onto the skull in the center of the headframe well. Mice were recovered for at least seven
908 days before ISI mapping. ISI was then used to measure the hemodynamic response to visual stimulation
909 across the entire field of view of a lightly anesthetized, head-fixed, mouse. The visual stimulus consisted

910 of sweeping a bar containing a flickering black-and-white checkerboard pattern across a grey
911 background[62]. To generate a map, the bar was swept across the screen ten times in each of the four
912 cardinal directions, moving at 9° per second. Processing of sign maps followed methods previously
913 described[63], with minor modifications. Phase maps were generated by calculating the phase angle of the
914 pre-processed DFT at the stimulus frequency. The phase maps were used to translate the location of a
915 visual stimulus displayed on the retina to a spatial location on the cortex. A sign map was produced from
916 the phase maps by taking the sign of the angle between the altitude and azimuth map gradients.
917 Averaged sign maps were produced from a minimum of three time series images, for a combined
918 minimum average of 30 stimulus sweeps in each direction. Visual area segmentation and identification
919 was obtained by converting the visual field map to a binary image using a manually-defined threshold and
920 further processing the initial visual areas with split/merge routine[63]. Sign maps were curated and the
921 experiment repeated if; (1) <6 visual areas were positively identified, (2) retinotopic metrics of V1 were out
922 of bounds (azimuth coverage within 60-100 degrees and altitude coverage within 35-60 degrees) or, (3)
923 auto-segmented maps needed to be annotated with more than 3 adjustments. Each animal had 3
924 attempts to get a passing map.

925 All mice received one unilateral injection into a single target region. For injections using stereotaxic
926 coordinates from bregma as a registration point, an incision was made to expose the skull and bregma
927 was visualized using a stereomicroscope. A hole overlying the targeted area was made by first thinning
928 the skull using a fine drill burr, then using a microprobe and fine forceps to remove the bone, revealing
929 the brain surface. For ISI-guided injections, the glass coverslip of the transcranial window was removed
930 by drilling around the edges and a small burr hole drilled, first through the Metabond and then through the
931 skull using surface vasculature fiducials obtained from the ISI session as a guide. An overlay of the sign
932 map over the vasculature fiducials was used to identify the target injection site. rAAV was delivered by
933 iontophoresis with current settings of 3 µA at 7 s 'on' and 7 s 'off' cycles for 5 min total, using glass
934 pipettes (inner tip diameters of 10–20 µm). Mice were perfused transcardially and brains collected 3
935 weeks post-injection for Cre mice.

936 *Serial two-photon tomography*
937 Imaging by serial two-photon (STP) tomography (TissueCyte 1000, TissueVision Inc. Somerville, MA) has
938 been described[4,27], and here we used the exact same procedures as our earlier published studies[4,25].

939 *Image data processing*
940 STP images were processed using the informatics data pipeline (IDP), which manages the processing
941 and organization of the image and quantified data for analysis and display in the web application as
942 previously described[4,28]. The two key algorithms are signal detection and image registration.

943 The signal detection algorithm was applied to each image to segment positive fluorescent signals from
944 background. Image intensity was first rescaled by square root transform to remove second-order effects
945 followed by histogram matching at the midpoint to a template profile. Median filtering and large kernel low
946 pass filter was then applied to remove noise. Signal detection on the processed image was based on a
947 combination of adaptive edge/line detection and morphological processing. Two variations of the
948 algorithm were employed, depending on the virus used for that experiment; one was tuned for EGFP, and
949 one for SypEGFP detection. High-threshold edge information was combined with spatial distance-
950 conditioned low-threshold edge results to form candidate signal object sets. The candidate objects were
951 then filtered based on their morphological attributes such as length and area using connected component
952 labelling. For the SypEGFP data, filters were tuned to detect smaller objects (punctate terminal boutons
953 vs long fibers). In addition, high intensity pixels near the detected objects were included into the signal
954 pixel set. Detected objects near hyper-intense artifacts occurring in multiple channels were removed. We
955 developed an additional filtering step using a supervised decision tree classifier to filter out surface
956 segmentation artifacts (**Supplemental Figure 9**), based on morphological measurements, location
957 context and the normalized intensities of all three channels.

958 The output is a full resolution mask that classifies each 0.35 μm × 0.35 μm pixel as either signal or
959 background. An isotropic 3-D summary of each brain is constructed by dividing each image into
960 10 μm × 10 μm grid voxels. Total signal is computed for each voxel by summing the number of signal-
961 positive pixels in that voxel. Each image stack is registered in a multi-step process using both global
962 affine and local deformable registration to the 3-D Allen mouse brain reference atlas as previously
963 described[28] . Segmentation and registration results are combined to quantify signal for each voxel in the
964 reference space and for each structure in the reference atlas ontology by combining voxels from the
965 same structure.

966 *Creation of the cortical top-down and flattened views of the CCF for data visualization.*
967 A standard z-projection of signal in a top-down view of the cortex mixes signal from multiple areas.
968 Visualizations of fluorescence in **Figures 1-3** instead project signal along a curved cortical coordinate
969 system that more closely matches the columnar structure of the cortex. This coordinate system was
970 created by first solving Laplace's equation between pia and white matter surfaces, resulting in
971 intermediate equi-potential surfaces. Streamlines were computed by finding orthogonal (steepest
972 descent) paths through the equi-potential field. Cortical signal can then be projected along these
973 streamlines for visualization.

974 A cortical flatmap was also constructed to enable visualization of anatomical and projection information
975 while preserving spatial context for the entire cortex. The flatmap was created by computing the geodesic
976 distance (the shortest path between two points on a curve surface) between every point on the cortical
977 surface and two pairs of selected anchor points. Each pair of anchor points form one axis of the 2D
978 embedding of the cortex into a flatmap. The 2D coordinate for each point on the cortical surface is
979 obtained by finding the location such that the radial (circular) distance from the anchor points (in 2D)
980 equals to the geodesic distance that was computed in 3D. This procedure produces smooth mapping of
981 the cortical surface onto a 2D plane for visualization. This embedding does not preserve area and the
982 frontal pole and medial-posterior region is highly distorted. As such, all numerical computation is done in
983 3D space. Similar techniques are used for texture mapping on geometric models in the field of computer
984 graphics[64].

985 *Data availability*
986 Data (high resolution images, segmentation, registration to CCF, automated quantification) are available
987 through the Allen Mouse Brain Connectivity Atlas portal (http://connectivity.brain-map.org/). In addition to
988 visualization and search tools available at this site, users can also download data using the Allen Brain
989 Atlas API (http://help.brain-map.org/display/mouseconnectivity/API) and the Allen Brain Atlas Software
990 Development Kit (SDK: http://alleninstitute.github.io/AllenSDK/connectivity.html). Through the SDK,
991 structure and voxel-level projection data is available for download. Examples of code for common data
992 requests are provided as part of the Mouse Connectivity Jupyter notebook to help users get started with
993 their own data analyses.

994 *Network modularity analysis*
995 The matrix of connection weights between cortical areas (**Figure 2b**) was obtained from a novel model[31].
996 Briefly, this model allows us to predict the structural connectivity strengths between any given brain
997 region in the mouse at the scale of voxels. This model combines the information from the 'wild type' viral
998 tracing experiments performed as a part of the Allen Mouse Brain Connectivity Atlas. It uses the spatial
999 information given by distances to injection sites to infer a connectivity strength from a given voxel to every
1000 other voxel in the Allen CCF.

1001 We analyzed the network structure of this graph using the Louvain Community Detection algorithm from
1002 the Brain Connectivity Toolbox (https://sites.google.com/site/bctnet/)[32,65]. The Louvain algorithm uses a
1003 greedy algorithm to define groups of nodes (modules) that are more connected to each other than they
1004 are to other nodes outside their module. We determined the modularity at various levels of granularity by
1005 varying the resolution parameter, γ, from 0-2.5 in steps of 0.1. For each value of γ, the modularity was

1006 computed 1000x and each pair of regions received an affinity score between 0 and 1. The affinity score is
1007 the probability of two regions being assigned to the same module weighted by the modularity score (Q)
1008 for that iteration, thereby assigning higher weights to partitions with a higher modularity score. Each
1009 region was assigned to the module with which it had the highest affinity, with the caveat that all structures
1010 within a module had an affinity score >= 0.5 with all other members of the module. For each value of γ, we
1011 also generated a shuffled matrix containing the same weights but with the source and target regions
1012 randomized. The modularity for the cortical and hippocampal matrix (Q) and the shuffled matrix (Q$_{shuffled}$)
1013 were evaluated at each value of γ.

1014 *Clustering Analyses and Statistics*
1015 Unsupervised hierarchical clustering was conducted with the online software, Morpheus,
1016 (https://software.broadinstitute.org/morpheus/) for algorithms and for visualization of the dendrogram and
1017 heat maps. Log-transforms were calculated on all values after adding a small value (0.5 minimum of the
1018 true positive array elements) to avoid Log (0). Proximity between clusters was computed using average
1019 linkages with spearman rank correlations as the distance metric. The clustering algorithm works
1020 agglomeratively: initially assigning each sample to its own cluster and iteratively merging the most
1021 proximal pair of clusters until finally all the clusters have been merged. To compare distances between
1022 granular and agranular samples (those that lack a L4), the computation of the distance metric was
1023 restricted to the set of shared layer projection fractions. In other words, we used the set of projection
1024 fractions in all layers when evaluating granular-granular distances, whereas when evaluating agranular-
1025 agranular or agranular-granular cortex, we used the set of all layers except L4. The software program
1026 GraphPad Prism was used for statistical tests and generation of all graphs, and the software program
1027 Gephi was used for visualization and layout of network diagrams.

1028 *Unsupervised discovery of hierarchy position*
1029 Following the classification of the laminar patterns in clusters, we use an unsupervised method to
1030 simultaneously assign a direction to a cluster type and to construct a hierarchy.

1031 First consider a mapping function

1032
$$M: [1, c] \sqcap N \rightarrow \{-1, 1\}$$

1033 which maps a type of connection cluster to either feedforward (M=1) or feedback (M=-1) type. We search
1034 over the space of possible maps to see which map produces the most self-consistent hierarchy. Since
1035 some transgenic line have different numbers of connections in different clusters, some maps will lead to
1036 particular transgenic lines having very biased feedforward or feedback calls. Thus, we add a confidence
1037 measure, which decreases the importance of the information provided by a transgenic line to the global
1038 hierarchy if the calls from that transgenic line are biased.

1039
$$conf(T) = 1 - \left| \langle M(C_{T_{i,j}}) \rangle_{i,j} \right| \tag{1}$$

1040 with a global confidence as an average over all the inter-areal connections above the threshold (10^-1.5)

1041
$$confg = \langle conf(T) \rangle_{i,j} \tag{2}$$

1042 We define the hierarchical position of a source area based on the difference between the feedback and
1043 feedforward connections originating from this area, normalized by the number of connections, which is
1044 normalized by the confidence we have from different Cre lines providing information about the
1045 directionality of the connection. The hierarchical position as a target is the difference between the
1046 feedforward and feedback connections terminating in this area, normalized by the number of connections
1047 and confidence. The hierarchical position of an area is defined as the sum of these measures:

1048
$$H_i = \frac{1}{confg} \left(\langle M\left(C_{T_{i,j}}\right) \cdot conf(T) \rangle_j - \langle M\left(C_{T_{j,i}}\right) \cdot conf(T) \rangle_j \right) \tag{3}$$

28

1049   To test how self-consistent a hierarchy is we define the global hierarchy score:

1050

$$H = \frac{1}{2 \cdot confg} \langle M\left(C_{T_{i,j}}\right) \cdot conf(T) \cdot (H_i - H_j) \rangle_{i,j} \tag{4}$$

1051   We performed an exhaustive search over all the maps M for the entire set of cortico-cortical connections,
1052   and the most self-consistent hierarchy is obtained when connections of type 1,3 and 5 are of one type
1053   and 2,4 and 6 are of the opposite type. Based on the position of the sensory areas, we conclude that type
1054   1,3 and 5 are feedforward and 2,4 and 6 are feedback. It should be noted that a similar search inside of
1055   the visual module results in mapping connections 3 and 5 to feedforward and 1,2,4 and 6 to feedback.

References

1056

1057   1.   Sporns, O., Tononi, G. & Kötter, R. The Human Connectome: A Structural Description of the
1058   Human Brain. *PLoS Comput. Biol.* **1,** e42 (2005).

1059   2.   Bohland, J. W. *et al.* A Proposal for a Coordinated Effort for the Determination of Brainwide
1060   Neuroanatomical Connectivity in Model Organisms at a Mesoscopic Scale. *PLoS Comput. Biol.* **5,**
1061   e1000334 (2009).

1062   3.   Zingg, B. *et al.* Neural Networks of the Mouse Neocortex. *Cell* **156,** 1096–1111 (2014).

1063   4.   Oh, S. W. *et al.* A mesoscale connectome of the mouse brain. *Nature* **508,** 207–214 (2014).

1064   5.   Markov, N. T. *et al.* A weighted and directed interareal connectivity matrix for macaque cerebral
1065   cortex. *Cereb. Cortex* **24,** 17–36 (2014).

1066   6.   Bota, M., Sporns, O. & Swanson, L. W. Architecture of the cerebral cortical association
1067   connectome underlying cognition. *Proc. Natl. Acad. Sci.* **112,** E2093–E2101 (2015).

1068   7.   Scannell, J. W., Blakemore, C. & Young, M. P. Analysis of connectivity in the cat cerebral cortex.
1069   *J. Neurosci.* **15,** 1463–83 (1995).

1070   8.   Swanson, L. W., Hahn, J. D. & Sporns, O. Organizing principles for the cerebral cortex network of
1071   commissural and association connections. *Proc. Natl. Acad. Sci.* **114,** E9692–E9701 (2017).

1072   9.   Bullmore, E. & Sporns, O. Complex brain networks: graph theoretical analysis of structural and
1073   functional systems. *Nat. Rev. Neurosci.* **10,** 186–198 (2009).

1074   10.   Sporns, O. *Connectome Networks: From Cells to Systems. Micro-, Meso- and Macro-*
1075   *Connectomics of the Brain* (Springer, 2016). doi:10.1007/978-3-319-27777-6_8

1076   11.   Wang, Q., Sporns, O. & Burkhalter, A. Network analysis of corticocortical connections reveals
1077   ventral and dorsal processing streams in mouse visual cortex. *J. Neurosci.* **32,** 4386–99 (2012).

1078   12.   Felleman, D. J. & Van Essen, D. C. Distributed Hierarchical Processing in the Primate Cerebral
1079   Cortex. *Cereb. Cortex* **1,** 1–47 (1991).

1080   13.   Rockland, K. S. & Pandya, D. N. Laminar origins and terminations of cortical connections of the
1081   occipital lobe in the rhesus monkey. *Brain Res.* **179,** 3–20 (1979).

1082   14.   Riesenhuber, M. & Poggio, T. Hierarchical models of object recognition in cortex. *Nat. Neurosci.* **2,**
1083   1019–1025 (1999).

1084   15.   Tasic, B. *et al.* Adult mouse cortical cell taxonomy revealed by single cell transcriptomics. *Nat.*
1085   *Neurosci.* **19,** 335–346 (2016).

1086   16.   Tasic, B. *et al.* Shared and distinct transcriptomic cell types across neocortical areas. *bioRxiv*
1087   229542 (2017). doi:10.1101/229542

1088   17.   Zeng, H. & Sanes, J. R. Neuronal cell-type classification: challenges, opportunities and the path
1089   forward. *Nat. Rev. Neurosci.* **18,** 530–546 (2017).

1090   18.   Sorensen, S. A. *et al.* Correlated gene expression and target specificity demonstrate excitatory
1091   projection neuron diversity. *Cereb. Cortex* **25,** 433–449 (2015).

1092   19.   Shepherd, G. M. G. Corticostriatal connectivity and its role in disease. *Nat. Rev. Neurosci.* **14,**
1093   278–291 (2013).

1094   20.   Harris, K. D. & Shepherd, G. M. G. The neocortical circuit: themes and variations. *Nat. Neurosci.*
1095   **18,** 170–181 (2015).

1096   21.   Gong, S. *et al.* Targeting Cre Recombinase to Specific Neuron Populations with Bacterial Artificial
1097   Chromosome Constructs. *J. Neurosci.* **27,** 9817–9823 (2007).

1098   22.   Gerfen, C. R., Paletzki, R. & Heintz, N. GENSAT BAC Cre-Recombinase Driver Lines to Study the
1099   Functional Organization of Cerebral Cortical and Basal Ganglia Circuits. *Neuron* **80,** 1368–1383
1100   (2013).

1101   23.   Harris, J. A. *et al.* Anatomical characterization of Cre driver mice for neural circuit mapping and
1102   manipulation. *Front. Neural Circuits* **8,** 1–16 (2014).

1103   24.   Daigle, T. L. *et al.* A suite of transgenic driver and reporter mouse lines with enhanced brain cell
1104   type targeting and functionality. *bioRxiv* 224881 (2017). doi:10.1101/224881

1105   25.   Martersteck, E. M. *et al.* Diverse Central Projection Patterns of Retinal Ganglion Cells. *Cell Rep.*
1106   **18,** 2058–2072 (2017).

1107   26.   Coogan, T. A., Burkhalter, A. & Martin, K. Hierarchical organization of areas in rat visual cortex. *J.*
1108   *Neurosci.* **13,** 3749–72 (1993).

1109   27.   Ragan, T. *et al.* Serial two-photon tomography for automated ex vivo mouse brain imaging. *Nat.*
1110   *Methods* **9,** 255–8 (2012).

1111   28.   Kuan, L. *et al.* Neuroinformatics of the allen mouse brain connectivity atlas. *Methods* **73,** 4–17
1112   (2015).

1113   29.   Kim, E. J., Juavinett, A. L., Kyubwa, E. M., Jacobs, M. W. & Callaway, E. M. Three Types of
1114   Cortical Layer 5 Neurons That Differ in Brain-wide Connectivity and Function. *Neuron* **88,** 1253–
1115   1267 (2015).

1116   30.   Olsen, S. R., Bortone, D. S., Adesnik, H. & Scanziani, M. Gain control by layer six in cortical
1117   circuits of vision. *Nature* **483,** 47–52 (2012).

1118   31.   Knox, J. E. *et al.* High resolution data-driven model of the mouse connectome. *bioRxiv* 293019
1119   (2018). doi:10.1101/293019

1120   32.   Rubinov, M. & Sporns, O. Complex network measures of brain connectivity: Uses and
1121   interpretations. *Neuroimage* **52,** 1059–1069 (2010).

1122   33.   Sporns, O. & Betzel, R. F. Modular Brain Networks. *Annu. Rev. Psychol.* **67,** 613–640 (2016).

1123   34.   Ria Ercsey-Ravasz, M. *et al.* A Predictive Network Model of Cerebral Cortical Connectivity Based
1124   on a Distance Rule. *Neuron* **80,** 184–197 (2013).

1125   35.   Jacomy, M., Venturini, T., Heymann, S. & Bastian, M. ForceAtlas2, a Continuous Graph Layout
1126   Algorithm for Handy Network Visualization Designed for the Gephi Software. *PLoS One* **9,** e98679
1127   (2014).

1128   36.   Gămănuţ, R. *et al.* The Mouse Cortical Connectome, Characterized by an Ultra-Dense Cortical
1129   Graph, Maintains Specificity by Distinct Connectivity Profiles. *Neuron* **97,** 698–715.e10 (2018).

1130   37.   Markov, N. T. *et al.* Weight Consistency Specifies Regularities of Macaque Cortical Networks.
1131   *Cereb. Cortex* **21,** 1254–1272 (2011).

1132 38. Maunsell, J. H. & van Essen, D. C. The connections of the middle temporal visual area (MT) and
1133   their relationship to a cortical hierarchy in the macaque monkey. *J. Neurosci.* **3,** 2563–86 (1983).

1134 39. Markov, N. T. *et al.* Anatomy of hierarchy: Feedforward and feedback pathways in macaque visual
1135   cortex. *J. Comp. Neurol.* **522,** 225–259 (2014).

1136 40. D'Souza, R. D., Meier, A. M., Bista, P., Wang, Q. & Burkhalter, A. Recruitment of inhibition and
1137   excitation across mouse visual cortex depends on the hierarchy of interconnecting areas. *Elife* **5,**
1138   e19332 (2016).

1139 41. D'Souza, R. D. & Burkhalter, A. A Laminar Organization for Selective Cortico-Cortical
1140   Communication. *Front. Neuroanat.* **11,** 1–13 (2017).

1141 42. Marshel, J. H., Garrett, M. E., Nauhaus, I. & Callaway, E. M. Functional Specialization of Seven
1142   Mouse Visual Cortical Areas. *Neuron* **72,** 1040–1054 (2011).

1143 43. Huh, C. Y. L., Peach, J. P., Bennett, C., Vega, R. M. & Hestrin, S. Feature-Specific Organization of
1144   Feedback Pathways in Mouse Visual Cortex. *Curr. Biol.* **28,** 114–120.e5 (2018).

1145 44. Zhang, S. *et al.* Selective attention. Long-range and local circuits for top-down modulation of visual
1146   cortex processing. *Science* **345,** 660–5 (2014).

1147 45. Leinweber, M., Ward, D. R., Sobczak, J. M., Attinger, A. & Keller, G. B. A Sensorimotor Circuit in
1148   Mouse Cortex for Visual Flow Predictions. *Neuron* **95,** 1420–1432.e5 (2017).

1149 46. Wang, Q., Sporns, O. & Burkhalter, A. Network Analysis of Corticocortical Connections Reveals
1150   Ventral and Dorsal Processing Streams in Mouse Visual Cortex. *J. Neurosci.* **32,** 4386–4399
1151   (2012).

1152 47. Carlén, M. What constitutes the prefrontal cortex? *Science* **358,** 478–482 (2017).

1153 48. Avery, J. A. *et al.* Convergent gustatory and viscerosensory processing in the human dorsal mid-
1154   insula. *Hum. Brain Mapp.* **38,** 2150–2164 (2017).

1155 49. Hanamori, T., Kunitake, T., Kato, K. & Kannan, H. Responses of Neurons in the Insular Cortex to
1156   Gustatory, Visceral, and Nociceptive Stimuli in Rats. *J. Neurophysiol.* **79,** 2535–2545 (1998).

1157 50. Veinante, P. & Deschênes, M. Single-cell study of motor cortex projections to the barrel field in
1158   rats. *J. Comp. Neurol.* **464,** 98–103 (2003).

1159 51. Douglas, R. J. & Martin, K. A. C. NEURONAL CIRCUITS OF THE NEOCORTEX. *Annu. Rev.
1160   Neurosci.* **27,** 419–451 (2004).

1161 52. Fame, R. M., MacDonald, J. L. & Macklis, J. D. Development, specification, and diversity of
1162   callosal projection neurons. *Trends Neurosci.* **34,** 41–50 (2011).

1163 53. Yamins, D. L. K. & DiCarlo, J. J. Using goal-driven deep learning models to understand sensory
1164   cortex. *Nat. Neurosci.* **19,** 356–365 (2016).

1165 54. Rao, R. P. N. & Ballard, D. H. Predictive coding in the visual cortex: a functional interpretation of
1166   some extra-classical receptive-field effects. *Nat. Neurosci.* **2,** 79–87 (1999).

1167 55. Cain, N., Iyer, R., Koch, C. & Mihalas, S. The Computational Properties of a Simplified Cortical
1168   Column Model. *PLOS Comput. Biol.* **12,** e1005045 (2016).

1169 56. Coogan, T. A. & Burkhalter, A. Conserved patterns of cortico-cortical connections define areal
1170   hierarchy in rat visual cortex. *Exp. brain Res.* **80,** 49–53 (1990).

1171 57. Shipp, S. The importance of being agranular: a comparative account of visual and motor cortex.
1172   *Philos. Trans. R. Soc. B Biol. Sci.* **360,** 797–814 (2005).

1173 58. Kim, Y. *et al.* Brain-wide Maps Reveal Stereotyped Cell-Type-Based Cortical Architecture and

1174   Subcortical Sexual Dimorphism. *Cell* **171,** 456–469.e22 (2017).

1175 59.   Han, Y. *et al.* The logic of single-cell projections from visual cortex. *Nature* (2018).
1176   doi:10.1038/nature26159

1177 60.   Economo, M. N. *et al.* A platform for brain-wide imaging and reconstruction of individual neurons.
1178   *Elife* **5,** (2016).

1179 61.   Franklin, K. B. J. & Paxinos, G. *Paxinos and Franklin's The mouse brain in stereotaxic*
1180   *coordinates.* (2012).

1181 62.   Kalatsky, V. A. & Stryker, M. P. New paradigm for optical imaging: temporally encoded maps of
1182   intrinsic signal. *Neuron* **38,** 529–45 (2003).

1183 63.   Garrett, M. E., Nauhaus, I., Marshel, J. H. & Callaway, E. M. Topography and Areal Organization
1184   of Mouse Visual Cortex. *J. Neurosci.* **34,** 12587–12600 (2014).

1185 64.   Oliveira, G. N., Torchelsen, R. P., Comba, J. L. D., Walter, M. & Bastos, R. Geotextures: A Multi-
1186   source Geodesic Distance Field Approach for Procedural Texturing of Complex Meshes. in *2010*
1187   *23rd SIBGRAPI Conference on Graphics, Patterns and Images* 126–133 (IEEE, 2010).
1188   doi:10.1109/SIBGRAPI.2010.25

1189 65.   Blondel, V. D., Guillaume, J.-L., Lambiotte, R. & Lefebvre, E. Fast unfolding of communities in
1190   large networks. *J. Stat. Mech. Theory Exp.* **2008,** P10008 (2008).

1191